

Predicting parametric spatiotemporal dynamics by multi-resolution PDE structure-preserved deep learning

Xin-Yang Liu^a, Hao Sun^d, Jian-Xun Wang^{a,b,c,*}

^a*Department of Aerospace and Mechanical Engineering, University of Notre Dame, Notre Dame, IN*

^b*Lucy Family Institute for Data & Society, University of Notre Dame, Notre Dame, IN*

^c*Center for Sustainable Energy (ND Energy), University of Notre Dame, Notre Dame, IN*

^d*Gaoling School of Artificial Intelligence, Renmin University of China, Beijing*

Abstract

Although recent advances in deep learning (DL) have shown a great promise for learning physics exhibiting complex spatiotemporal dynamics, the high training cost, unsatisfying extrapolability for long-term predictions, and poor generalizability in out-of-sample regimes significantly limit their applications in science/engineering problems. A more promising way is to leverage available physical prior and domain knowledge to develop scientific DL models, known as physics-informed deep learning (PiDL). In most existing PiDL frameworks, e.g., physics-informed neural networks, the physics prior is mainly utilized to regularize neural network training by incorporating governing equations into the loss function in a soft manner. In this work, we propose a new direction to leverage physics prior knowledge by baking the mathematical structures of governing equations into the neural network architecture design. In particular, we develop a novel PDE-preserved neural network (PPNN) for rapidly predicting parametric spatiotemporal dynamics, given the governing PDEs are (partially) known. The discretized PDE structures are preserved in PPNN as convolutional residual network (ConvResNet) blocks, which are formulated in a multi-resolution setting. This physics-inspired learning architecture design endows PPNN with excellent generalizability and long-term prediction accuracy compared to the state-of-the-art blackbox ConvResNet baseline. The effectiveness and merit of the proposed methods have been demonstrated over a handful of spatiotemporal dynamical

*Corresponding author. Tel: +1 574-631-5302

Email address: jwang33@nd.edu (Jian-Xun Wang)

systems governed by unsteady PDEs, including reaction-diffusion, Burgers', and Navier-Stokes equations.

Keywords: Physics-informed deep learning, Scientific machine learning, Surrogate modeling, Operator learning, Residual connection, Computational fluid dynamics

1. Introduction

Computational modeling and simulation capabilities play an essential role in understanding, predicting, and controlling various physical processes (e.g., turbulence, heat-flow coupling, and fluid-structure interaction), which often exhibit complex spatiotemporal dynamics. These physical phenomena are usually governed by partial differential equations (PDEs) and can be simulated by solving these PDEs numerically based on, e.g., finite difference (FD), finite volume (FV), finite element (FE), or spectral methods. However, predictive modeling of complex spatiotemporal dynamics using traditional numerical methods can be significantly challenging in many practical scenarios: (1) governing equations for complex systems might not be fully known due to a lack of complete understanding of the underlying physics, for which a first-principled numerical solver cannot be built; (2) conventional numerical simulations are usually time-consuming, making it infeasible for many applications that require many repeated model queries, e.g., optimization design, inverse problems, and uncertainty quantification (UQ), attracting increasing attention in scientific discovery and engineering practice.

Recent advances in scientific machine learning (SciML) and ever-growing data availability open up new possibilities to tackle these challenges. In the past few years, various deep neural networks (DNNs) have been designed to learn the spatiotemporal dynamics in latent spaces enabled by proper orthogonal decomposition (POD) [1–6] or convolutional encoding-decoding operations [7–13]. In particular, fast neural simulators based on graph neural networks (GNN) have been proposed and demonstrated to predict spatiotemporal physics on irregular domains with unstructured meshes [14, 15]. Although showing good promise, most of these works are purely data-driven and black-box in nature, which rely on “big data” and may have poor generalizability, particularly in out-of-sample regimes in the parameter space. As a more promising strategy, baking physics prior knowledge (e.g., conservation laws, governing equations, and

constraints) into deep learning is believed to be very effective to improve its sample efficiency and generalizability [16], here referred to as physics-informed deep learning (PIDL). An impressive contribution in this direction is physics-informed neural networks (PINNs) [17], where well-posed PDE information is leveraged to enable deep learning in data-sparse regimes. The general idea of PINNs is to learn (or solve) the PDE solutions with DNNs, where the loss functions are formulated as a combination of the data mismatch and residuals of known PDEs, unifying forward and inverse problems within the same DNN optimization framework. The merits of PINNs have been demonstrated over various scientific applications, including fast surrogate/meta modeling [18–20], parameter/field inversion [21–24], and solving high-dimensional PDEs [25–27], to name a few. Due to the scalability challenges of the pointwise fully-connected PINN formulation to learn continuous functions [28–31] or operators [32–34], many remedies and improvements in terms of training and convergence have been proposed [35–37]. In particular, there is a growing trend in developing field-to-field discrete PINNs by leveraging convolution operations and numerical discretizations, which have been demonstrated to be more efficient in spatiotemporal learning [38, 39]. For example, convolution neural networks (CNN) or graph convolution networks (GCN) were built to approximate the discrete PDE solutions, where the PDE residuals can be formulated in either strong or weak forms by finite-difference [40–43], finite volume [44], or finite element methods [45–47]. Moreover, recurrent network formulation informed by discretized PDEs have been developed for spatiotemporal dynamic control using model-based reinforcement learning [48].

In the PINN framework, the term “physics-informed” mainly refers to imposing PDE residuals in the loss or likelihood functions to regularize/drive DNN training. However, it remains unclear how to leverage physics-induced bias, i.e., (partially) known governing equations, to inform the *learning architecture design*, which is the focus of this work. Recent studies have revealed the connection between neural network structures and ordinal/partial differential equations (ODEs/PDEs) [49–54]. For example, Lu et al. [50] bridged deep convolutional network architectures and numerical differential equations. Chen et al. [55] showed that the residual networks (ResNets) [56] can be interpreted as the explicit Euler discretization of an ODE,

while ODEs can be used to formulate the continuous residual connection with infinite depths, known as the NeuralODE [57]. Motivated by differential equations, novel deep learning architectures have been recently developed in the computer science community, e.g., new convolutional ResNets guided by parabolic and hyperbolic PDEs [52], GRAND as a graph network motivated by diffusion equations [53], and PDE-GCN motivated by hyperbolic PDEs to improve over-smooth issues in deep graph learning [54]. However, these studies mainly aimed to develop generic DNN architectures with some desired features by utilizing specific properties of certain PDEs (e.g., diffusion, dispersion, etc.), and the designed neural networks are not necessarily used to learn the physical processes governed by those PDEs. In this paper, we are interested in the design of novel learning architectures for predicting spatiotemporal dynamics by preserving their governing PDEs in the discrete forms as convolution operations. This study explores PIDL in novel learning architecture design, along the line of differentiable programming (∂P), which is a generic concept of extending DNNs to more general computer programs that can be trained in the same way as deep learning models do [58]. In general, a ∂P model is formulated by marrying DNNs with a fully differentiable physics-based solver, and thus the gradients can be back-propagated through the entire hybrid neural solver based on automatic differentiation (AD) or discrete adjoint methods. Relevant works include universal differential equations (UDE) [59], NeuralPDE [60], and others, where DNNs are formulated within a differentiable PDE solver for physics-based modeling. In particular, this idea has been recently explored in predictive modeling of rigid body dynamics [61, 62], epidemic dynamics [63], and fluid dynamics [64–66]. These studies imply great promise of incorporating physics-induced prior (i.e., PDE) into DNN architectures.

In this work, we propose a novel PDE structure-preserved deep learning framework for rapidly predicting parametric spatiotemporal dynamics, where the network architecture design is inspired by the governing PDEs, discretized in a multi-resolution setting. Specifically, we develop a new auto-regressive neural solver based on convolutional ResNet framework, where the residual connections are constructed by preserving the governing PDE structures, which are (partially) known *a priori*, discretized on low-resolution grids, while encoding-decoding con-

volution operations with trainable filters enable high-resolution state predictions on fine grids. Compared to classic ResNets with black-box residual connections, the proposed PDE-preserved neural network (PPNN) is expected to be superior in terms of both training efficiency and out-of-sample generalizability for, e.g., unseen boundary conditions and parameters, and extrapolating in time. The contributions of this work are summarized as follows: (i) an innovative physics-inspired learning architecture design is presented, where the PDE structures are preserved by the residual connection; (ii) multi-resolution information passing through network layers is proposed to stabilize long-term model rollout predictions over large time steps; (iii) the superiority of the proposed PPNN is demonstrated for PDE operator learning in terms of training complexity, extrapolability, and generalizability in comparison with the baseline black-box ResNet model, using a series of comprehensive numerical experiments on spatiotemporal dynamics governed by various parametric unsteady PDEs, including burgers equations, reaction-diffusion equations, and unsteady Navier-Stokes equations. The rest of the paper is organized as follows: the proposed structure of PPNN and its relationship with discretized governing PDEs are introduced in Section 2. Results of numerical experiments of three spatiotemporal dynamic problems with high-dimensional parameter space are presented in Section 3. In Section 4, we discuss more challenging scenarios where the prior physics knowledge is incomplete/inaccurate. Moreover, the training/inference cost and the role of the structure-preserving part in PPNN are discussed in detail. Finally, Section 5 concludes the paper.

2. Methodology

2.1. Problem formulation

We are interested in predictive modeling of physical systems with spatiotemporal dynamics, which can be described by a set of parametric coupled PDEs in the general form,

$$\frac{\partial \mathbf{u}}{\partial t} + \mathcal{F} \left[\mathbf{u}, \mathbf{u}^2, \dots, \nabla_x \mathbf{u}, \nabla_x^2 \mathbf{u}, \nabla_x \mathbf{u} \cdot \mathbf{u}, \dots; \boldsymbol{\lambda} \right] = \mathbf{0}, \quad \mathbf{x}, t \in \Omega \times [0, T], \boldsymbol{\lambda} \in \mathbb{R}^d, \quad (1a)$$

$$\mathcal{I} \left[\mathbf{x}, \mathbf{u}, \nabla_x^2 \mathbf{u}, \nabla_x \mathbf{u} \cdot \mathbf{u}; \boldsymbol{\lambda} \right] = \mathbf{0}, \quad \mathbf{x} \in \Omega, t = 0, \boldsymbol{\lambda} \in \mathbb{R}^d, \quad (1b)$$

$$\mathcal{B} \left[t, \mathbf{x}, \mathbf{u}, \nabla_x^2 \mathbf{u}, \nabla_x \mathbf{u} \cdot \mathbf{u}; \boldsymbol{\lambda} \right] = \mathbf{0}, \quad \mathbf{x}, t \in \partial\Omega \times [0, T], \boldsymbol{\lambda} \in \mathbb{R}^d, \quad (1c)$$

where $\mathbf{u} = \mathbf{u}(\mathbf{x}, t; \boldsymbol{\lambda}) \in \mathbb{R}^n$ is the n -dimensional state variable; t denotes time and $\mathbf{x} \in \Omega$ specifies the space; $\mathcal{F}[\cdot]$ is a complex nonlinear functional governing the physics, while differential operators $\mathcal{I}[\cdot]$ and $\mathcal{B}[\cdot]$ describe the initial and boundary conditions (I/BCs) of the system, respectively; $\boldsymbol{\lambda} \in \mathbb{R}^d$ is a d -dimensional vector, representing physical/modeling parameters in the governing PDEs and/or I/BCs. Solving this parametric spatiotemporal PDE system typically relies on traditional FD/FV/FE methods, which are computationally expensive in most cases. This is due to the spatiotemporal discretization of the PDEs into a high-dimensional algebraic system, making the numerical simulation time-consuming, particularly considering that a tiny step is often required for the time integration to satisfy the numerical stability constraint. Moreover, as the system solution $\mathbf{u}(\mathbf{x}, t; \boldsymbol{\lambda})$ is parameter-dependent, we have to start over and conduct the entire simulation given a new parameter $\boldsymbol{\lambda}$, making it infeasible for application scenarios that require many model queries, e.g., parameter inference, optimization, and uncertainty quantification. Therefore, our objective is to develop a data-driven neural solver for rapid spatiotemporal prediction, enabled by efficient time-stepping with coarse-gaining and fast inference speed of neural networks. In particular, this study focuses on the learning architecture design by preserving known PDE structures for improving the robustness, stability, and generalizability of data-driven auto-regressive predicting models.

2.2. Next-step prediction models based on convolutional ResNets

The next-step DNN predictors are commonly used for emulating spatiotemporal dynamics in an autoregressive manner,

$$\mathbf{u}_t = f_{\theta}(\mathbf{u}_{t-1}, \boldsymbol{\lambda} | \boldsymbol{\theta}), \quad (2)$$

where the state solution \mathbf{u}_t at time step t is approximated by a neural network function $f_{\theta} : \mathbb{R}^n \times \mathbb{R}^d \rightarrow \mathbb{R}^n$, taking the previous state \mathbf{u}_{t-1} and physical parameters $\boldsymbol{\lambda}$ as the input features. The function $f_{\theta}(\cdot | \boldsymbol{\theta})$ is parameterized by trainable weight vector $\boldsymbol{\theta}$ that can be optimized based on training labels. Once the model is fully trained, it can be used to predict spatiotemporal dynamics by autoregressive model rollouts given only the initial condition \mathbf{u}_0 and a specific set of physical parameters $\boldsymbol{\lambda}$. In general, the next-step model is built based on residual network (ResNet) blocks, which have recently improved the state-of-the-art (SOTA) in many benchmarks

learning tasks [14]. Given the input features z_0 , a ResNet block with N layers outputs z_N as,

$$z_{j+1} = z_j + f^{(j)}(z_j | \theta^{(j)}), \quad j = 0, \dots, N-1, \quad (3)$$

where $f^{(j)}$ represents the generic neural network function of j^{th} layer and $\theta^{(j)}$ are corresponding weights. For end-to-end spatiotemporal learning, $f^{(j)}$ are often formulated by (graph) convolutional neural networks with trainable convolution stencils and biases. In a ResNet block, the dimension of the feature vectors (i.e., the image resolution and the number of channels) should remain the same across all layers. The ResNet-based next-step models have been demonstrated powerful and effective for predicting complex spatiotemporal physics. One of the examples is the MeshGraphNet [14], which is a GNN-based ResNets and shows the SOTA performance in spatiotemporal learning with unstructured mesh data.

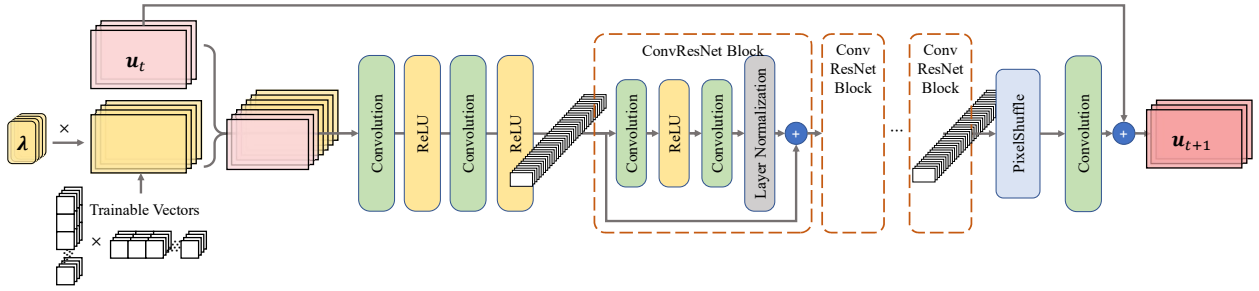


Figure 1: Network architecture of the baseline black-box ConvResNet-based next-step model.

In this work, as we limit ourselves to structured data within regular domains, a CNN variant of the MeshGraphNet, Convolutional ResNet (ConvResNet)-based next-step model, is used as the baseline black-box model in this work, whose network structure is shown in Fig. 1. The ConvResNet takes the previous state and physical parameters as the input and predicts the next-step state using a residual connection across the entire hidden ConvResNet layers after a pixel shuffle layer. The hidden layers consist of several ConvResNet blocks, constructed based on standard convolution layers with residual connections and ReLU activation functions, followed by layer normalization. To learn the dependence of physical parameters λ , each scalar component of the physical parameter vector is multiplied by a trainable matrix, which is obtained by vector multiplication of trainable weight vectors.

2.3. Neural network architecture and differential equations

Recent studies have shown the relationship between DNN architectures and differential equations: ResNets can be interpreted as discretized forms of ODEs/PDEs, while differential equations can be treated as a continuous interpretation of ResNet blocks with infinite depth.

Residual Connections and ODEs. As discussed in [49, 55], the residual connection as defined in Eq. 3 can be seen as a forward Euler discretization of a ODE,

$$\frac{\partial z(t)}{\partial t} = F(z(t) | \theta(t)), \quad \text{for } t \in (0, T], \quad (4)$$

where $z(t=0) = z_0$ and T is total time. In ResNets, a fixed time step size of $\Delta t = 1$ is set for the entire time span and $N \cdot \Delta t = T$. Namely, the depth of the residual connection (i.e., the number of layers in a ResNet block) can be controlled by changing the total time T . On the other hand, an ODE as given by Eq. 4 can be interpreted as a continuous ResNet block with infinite number of layers (i.e., infinite depth). Based on this observation, the classic ResNet structure can be extended by discretizing an ODE using different time-stepping schemes (e.g., Euler, Runge-Kutta, leapfrog, etc.). Moreover, we can also define a residual connection block by directly coupling a differentiable ODE solver with a multi-layer perception (MLP) representing $F(\cdot)$, where the hybrid ODE-MLP is trained as a whole differentiable program using back-propagation, which is known as a neural-ODE block [55].

Convolution operations and PDEs. In the neuralODE, MLP is used to define $F(\cdot)$, which, however, can be any neural network structure in a general setting. When dealing with structured data (e.g., images, videos, physical fields), the features $z(t, \mathbf{x})$ can be seen as spatial fields, and convolution operations are often used to construct a CNN-based $F(\cdot)$. A profound relationship between convolutions and differentiations has been presented in [50, 67, 68]. Following the deep learning convention, a 2D convolution is defined as,

$$\text{conv}(z, h^{(\theta)}) = \int z(\mathbf{x}' - \mathbf{x}) h^{(\theta)}(\mathbf{x}) d\mathbf{x}, \quad (5)$$

where h represent convolution kernel parameterized by θ . Based on the order of sum rules, the kernel h can be designed to approximate any differential operator with prescribed order of

accuracy [69], and thus the convolution in Eq. 5 can be expressed as [54],

$$\text{conv}(z, h^{(\theta)}) = \mathcal{D} \left[\mathbf{u}, \dots, \nabla_x \mathbf{u}, \nabla_x^2 \mathbf{u}, \nabla_x \mathbf{u} \cdot \mathbf{u}, \dots; \boldsymbol{\theta} \right], \quad (6)$$

where \mathcal{D} is a discrete differential operator based FD/FV/FE methods. For example, from the point of view of FDM, convolution filters can be seen as the finite difference stencils of certain can be interpreted as the discrete forms of certain PDEs, and thus the PDEs can be used to inform ConvResNet architecture design.

2.4. Multi-resolution PDE-preserved neural network (PPNN) architecture

It is well known that auto-regressive models suffer from error accumulation, which is particularly severe for the next-step formulation. Although remedies such as using training noises [70] or sequence models [15] have been explored, the error accumulation issue cannot be easily mitigated, and the model usually fails to operate in a long-span rollout. Inspired by the relationship between network architectures and differential equations, we *hypothesize* that the performance of an auto-regressive ConvResNet model for spatiotemporal learning can be significantly improved if the network is constructed by preserving (partially) known governing physics (i.e., PDEs) of the spatiotemporal dynamics. Therefore, we propose a multi-resolution PDE-preserved neural network (PPNN) framework, where the discrete governing PDEs are preserved in residual connection blocks using grids with multiple resolutions. As shown in Fig. 2, the PPNN has the same backbone ResNet structure as the black-box next-step baseline model, where a residual connection is applied across the entire hidden ConvResNet layers. The hidden ConvResNet consists of two portions: PDE-preserving ConvRes layers and trainable ConvRes layers, coupled in an encoding-decoding manner. In the PDE-preserving portion, the ConvRes connection is constructed based on the convolution operators defined by the discrete differential operators of the governing PDEs using finite-difference stencils. The preserved-PDE ConvRes layers are operated on low-resolution grids by taking in the bilinearly-downsampled input solution fields, which improves the model rollout stability with large evolving steps, meanwhile reducing the cost overhead during the model inference. The trainable portion takes the high-resolution solution fields as the input and contains a few classic ConvResNet blocks. For a fair

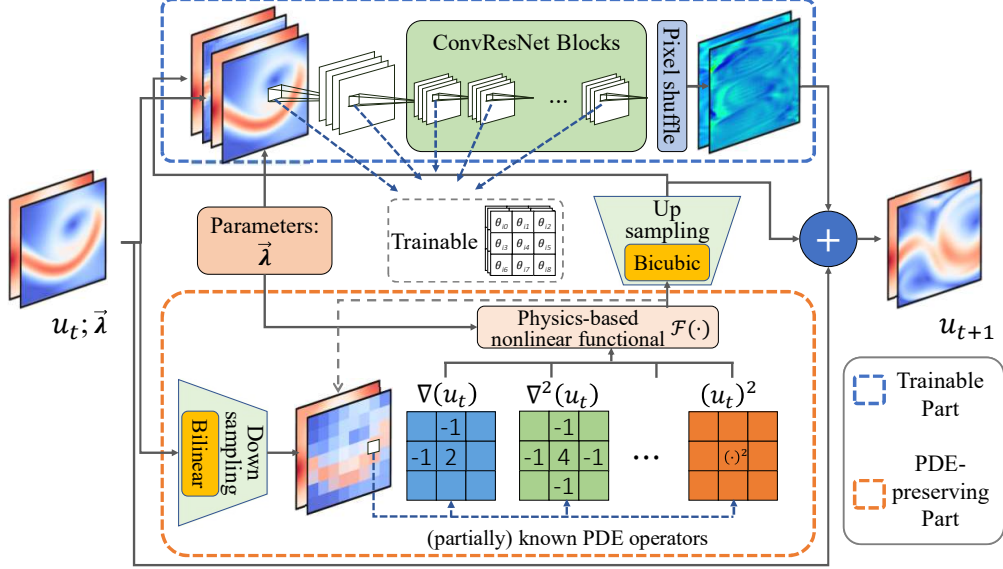


Figure 2: Schematic of the proposed multi-resolution PDE-preserved neural network (PPNN).

comparison, the network architecture of the trainable portion is exactly the same as that of the black-box ConvResNet baseline. The PDE-preserving part and trainable part are connected via bi-cubic up-sampling operation. Note that a smaller time step $\Delta t'$ can be used within the PDE-preserving portion via inner-iteration to stabilize model rollout. In general, the combination of the two portions can be seen as a new ConResNet architecture that preserves the mathematical structure of the underlying physics behind the spatiotemporal dynamics to be modeled.

3. Results

In this section, we evaluate the proposed PDE structure-preserved neural network (PPNN) on three nonlinear systems with spatiotemporal dynamics, where the governing PDEs are known *a priori*. Specifically, the spatiotemporal dynamics governed by FitzHugh-Nagumo reaction diffusion (RD) equations, Burgers' equations, and incompressible Navier-Stokes (NS) equations with varying parameters λ (e.g., IC, diffusion coefficients, Reynolds number, etc.) in 2D domains are studied. To demonstrate the merit of preserving the discrete PDE structure in ConvResNet, the proposed PPNN is compared with the baseline black-box ConvResNet next-step model (a CNN variant of the SOTA MeshGraphNet, see Sec. 2.2). As mentioned above, the net-

work architecture of the trainable portion of the PPNN is the same as the black-box baseline model for a fair comparison (except that the trainable portion of PPNN takes the output of the PDE-preserving part as an extra information.). Moreover, we use the same network setting, i.e., same network structure, hyperparameters and training epochs, for all the test cases (except for the NS system, which has slight modifications adapting to three state variables). In particular, the encoder consists of two layers of convolutional layers, using a 6×6 kernel, with zero padding of 2 and a stride of 2. Afterwards, there are three ConvResNet blocks , each with a 5×5 kernel, 48 channels and a zero padding of 2 (see Fig. 1). In NS cases, four ConvResNet blocks are used, each of which has a 7×7 kernel, 96 channels and a zero padding of 3. The following decoder includes a pixelshuffle with upscale factor equals 4 and a convolution layer with a 5×5 kernel and zero padding of 2. All the neural networks are implemented on the deep learning platform PyTorch [71] and trained on a NVIDIA RTX A6000 GPU card.

All the DNN predictions are evaluated against the high-resolution fully converged numerical solutions as the reference using a full-field error metric ϵ_t defined at time t as,

$$\epsilon_t = \frac{1}{N} \sum_{i=1}^N \sqrt{\frac{\|f_{\theta}(\hat{\mathbf{u}}_{t-1}, \boldsymbol{\lambda}_i | \boldsymbol{\theta}) + \hat{\mathbf{u}}_{t-1} - \mathbf{u}_t(\boldsymbol{\lambda}_i)\|_2^2}{\|\mathbf{u}_t(\boldsymbol{\lambda}_i)\|_2^2}}, \quad (7)$$

where N indicates the number of the testing physical parameters $\boldsymbol{\lambda}_i$, $\mathbf{u}_t(\boldsymbol{\lambda}_i)$ is the reference solution at time step t corresponding to the physical parameter $\boldsymbol{\lambda}_i$, f_{θ} represents the trained neural network function with optimized weights $\boldsymbol{\theta}$, and $\hat{\mathbf{u}}_{t-1}$ represents the state predicted by the model at previous time step $t - 1$,

$$\begin{aligned} \hat{\mathbf{u}}_t &= f_{\theta}(\hat{\mathbf{u}}_{t-1}, \boldsymbol{\lambda}_i | \boldsymbol{\theta}) + \hat{\mathbf{u}}_{t-1}, \quad t \in [2, n] \\ \hat{\mathbf{u}}_1 &= f_{\theta}(\mathbf{u}_0(\boldsymbol{\lambda}_i), \boldsymbol{\lambda}_i | \boldsymbol{\theta}) + \mathbf{u}_0(\boldsymbol{\lambda}_i) \end{aligned} \quad (8)$$

where n is the number of testing steps, $\mathbf{u}_0(\boldsymbol{\lambda}_i)$ represents the initial condition given $\boldsymbol{\lambda}_i$.

3.1. FitzHugh–Nagumo reaction diffusion equations

We first consider a spatiotemporal dynamic system governed by the FitzHugh–Nagumo equations with periodic BCs, which is a generic model for excitable media. The main part of the FitzHugh–Nagumo model is reaction-diffusion (RD) equations,

$$\frac{\partial \mathbf{u}}{\partial t} = \gamma \nabla^2 \mathbf{u} + \mathbf{R}(\mathbf{u}), \quad t \in [0, T], \quad (9)$$

where $\mathbf{u} = [u(x, y, t), v(x, y, t)]^T \in \mathbb{R}^2$ are two interactive components, γ is the diffusion coefficient, and $\mathbf{R}(\mathbf{u}) = [R_u(u, v), R_v(u, v)]^T$ are source terms for the reaction,

$$\begin{aligned} R_u(u, v) &= u - u^3 - v + \alpha, \\ R_v(u, v) &= \beta(u - v), \end{aligned} \tag{10}$$

where $\alpha = 0.01$ represents the external stimulus and $\beta = 0.25$ is the reaction coefficient. The initial condition (IC) \mathbf{u}_0 is a random field and generated by randomly sampling from a normal distribution,

$$u(x, y, 0), v(x, y, 0) \sim \mathcal{N}(0, 1), \tag{11}$$

which is normalized to $[0, 1]$ with a bias of 0.1. Given different ICs and diffusion coefficients γ , varying dynamic spatial patterns of neuron activities can be simulated. Here, the next-step neural solvers are trained to learn and used to predict the spatiotemporal dynamics of varying modeling parameters (i.e., ICs and diffusion coefficients). Namely, we attempt to build a surrogate model in a very high-dimensional parameter space $\boldsymbol{\lambda} \in \mathbb{R}^d$, where $d = 65,537$, since the dimensions for IC and diffusion coefficient are 256^2 and 1, respectively. The reference solutions are obtained on the simulation domain $(x, y) \in [0, 6.4] \times [0, 6.4]$, discretized with a fine mesh of 256×256 grids, based on the finite difference method, where spatial derivatives are computed by the 6th order accuracy central difference scheme and time stepping is based on the forward Euler method with the time step of $\delta t = 1 \times 10^{-5}$. The reference solution snapshots at every other 200 timesteps are collected for the neural network training, and thus the timestep size of the neural model is $\Delta t = 200\delta t$. The whole training dataset includes trajectories of sparse reference solutions at 8 different γ uniformly distributed in $[0.6, 1.3]$ and each γ comes with 32 randomly generated ICs. In total, the training set contains 256 trajectories, and each trajectory includes 100 snapshots covering the temporal range of $T = 100\Delta t$, which starts from the 2001st numerical step. In PPNN, the PDE-preserving portion is defined on a coarse mesh of size 48×48 with the same learning timestep size as the trainable part ($\Delta t' = \Delta t = 200\delta t$).

Figure 3 shows the PPNN-predicted solution snapshots of the RD equations at four randomly selected test parameters (i.e., randomly generated ICs and unseen diffusion coefficients). The prediction results of the proposed PPNN (Fig. 3(b)) and baseline black-box ConvResNet

(Fig. 3(c)) are compared against the ground truth reference (Fig. 3(a)). It can be seen that both

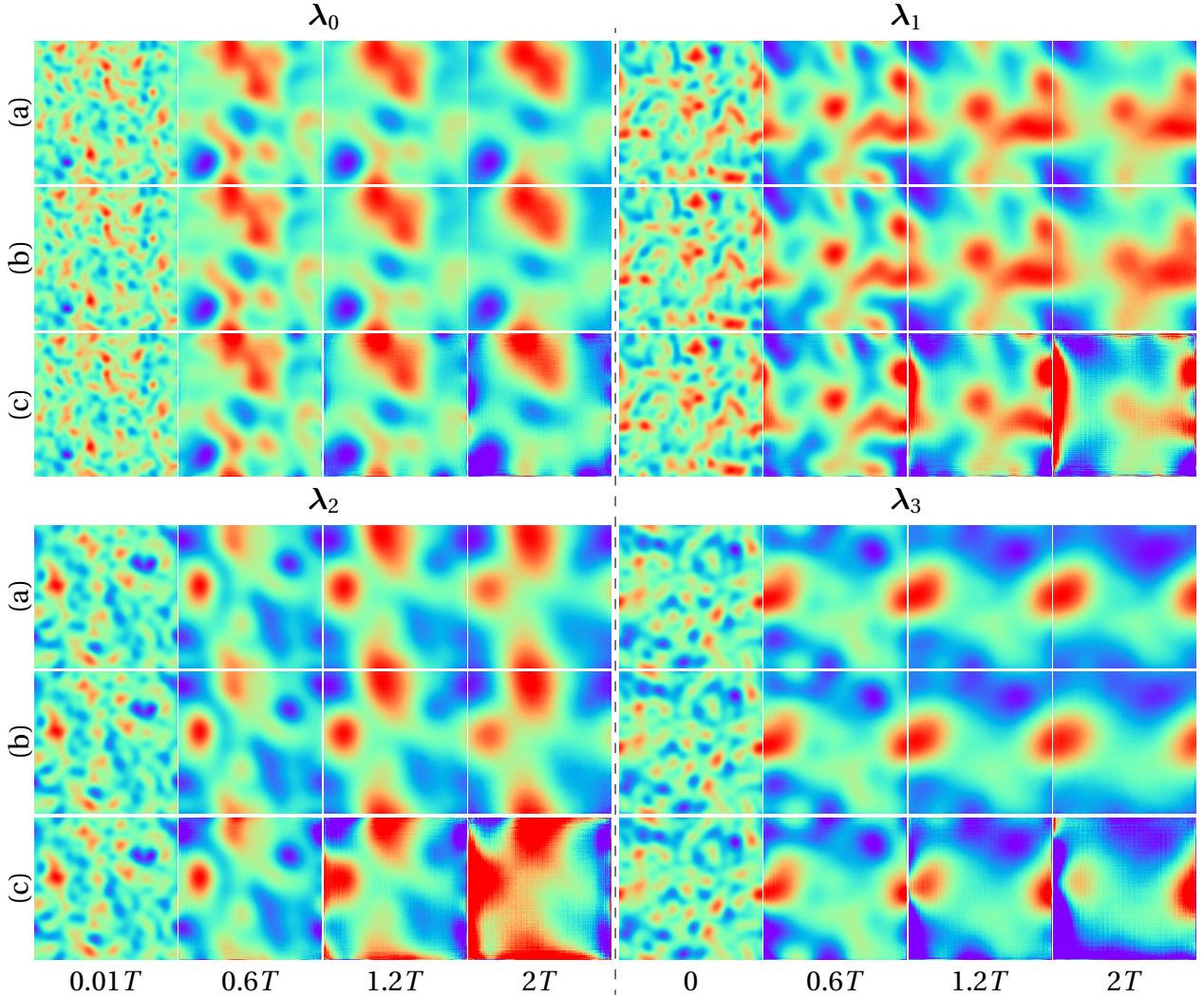


Figure 3: Predicted solution snapshots of u for the RD equations at different time steps and unseen parameters, obtained by (b) PPNN (our method) and (c) black-box ConvResNet (baseline model), compared against ground truth (high-resolution FD simulation). $\lambda_0, \lambda_1, \lambda_2$ and λ_3 are four randomly selected testing (unseen) parameters.

models agree with the reference solutions for $t < 0.6T$, showing good generalizability on testing ICs and γ for a short-term model rollout. However, the error accumulation becomes notable for the black-box baseline when $t > T$, and the spatial patterns of the baseline predictions significantly differ from the reference at $t = 2T$, which is an expected issue for the next-step predictors. In contrast, the results of our PPNN have an excellent agreement with the reference solutions over the entire time span $[0, 2T]$ on all testing parameters, showing great robustness,

predictability, and generalizability in both the spatiotemporal domain and parameter space. To

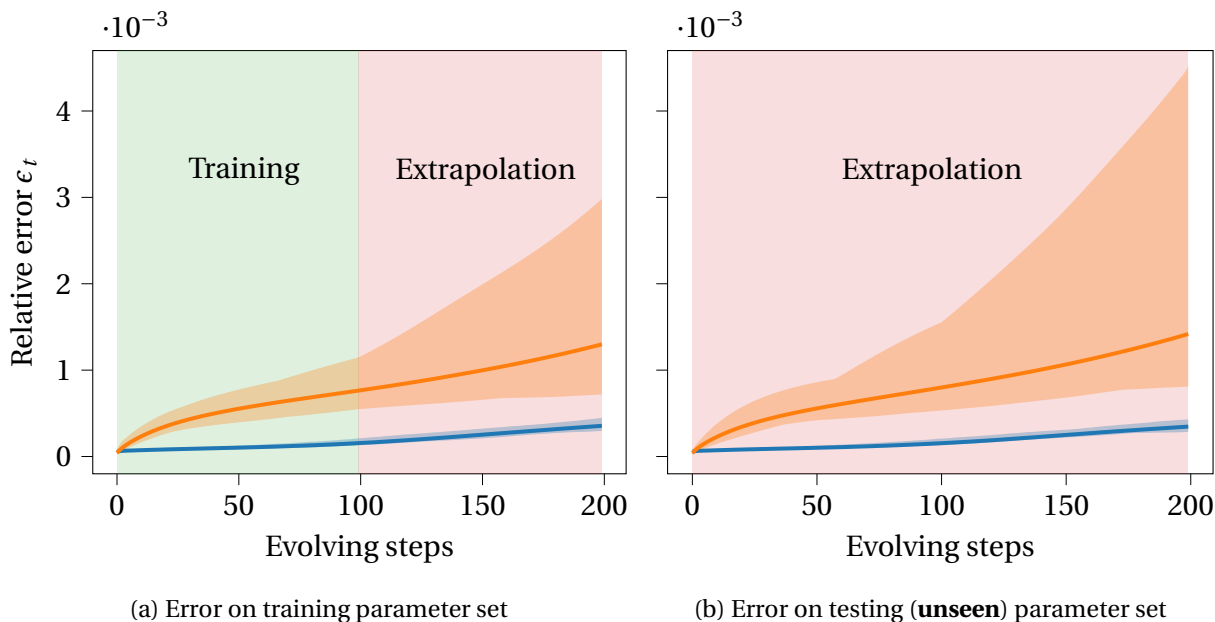


Figure 4: Relative prediction error ϵ_t of PPNN (—) and black-box ConvResNet baseline (—) for the RD dynamics, averaged on 100 randomly sampled (a) training parameters λ and (b) testing (*unseen*) parameters. The shaded area shows the maximum and minimum relative errors of all testing trajectories.

further examine the error propagation in time for both models, the relative testing errors ϵ_t averaged over 100 randomly selected parameters in training and testing sets are computed and plotted in Fig. 4, where the panel (a) shows the averaged model-rollout error evaluated on 100 training parameters and panel (b) shows the error averaged on 100 randomly generated testing parameters. The model is only trained within the range of $1T$ ($100\Delta t$), and it is clearly seen that the rollout error of the black-box model notably grows in the extrapolation range $[T, 2T]$ (from $100\Delta t$ to $200\Delta t$). The error accumulation becomes more severe for the unseen testing parameters. However, our PPNN predictions maintain an impressively low error, even when extrapolating twice the length of the training range. Besides, the uncertainty range of the error ensemble is significantly reduced compared to that of the black-box baseline, indicating great robustness of the proposed PPNN for different testing parameters.

3.2. 2D Burgers' equation

For the second case, we study the spatiotemporal dynamics governed by the viscous Burgers' equations on a 2D domain with periodic boundary conditions,

$$\frac{\partial \mathbf{u}}{\partial t} + \mathbf{u} \cdot \nabla \mathbf{u} = \nu \nabla^2 \mathbf{u}, \quad t \in [0, T], \quad (12)$$

where $\mathbf{u} = [u(x, y, t), v(x, y, t)]^T \in \mathbb{R}^2$ is the velocity vector, and ν represents the viscosity. The initial condition (IC) \mathbf{u}_0 is generated according to,

$$\mathbf{u}_0 = \begin{cases} u_0 = \sum_{i=-4}^4 \sum_{j=-4}^4 r_{i,j}^{(1)} \sin(ix + jy) + r_{i,j}^{(2)} \cos(ix + jy) \\ v_0 = \sum_{i=-4}^4 \sum_{j=-4}^4 r_{i,j}^{(3)} \sin(ix + jy) + r_{i,j}^{(4)} \cos(ix + jy) \end{cases} \quad r_{i,j}^{(1)}, r_{i,j}^{(2)} \sim \mathcal{N}(0, 1), \quad (13)$$

where x, y are spatial coordinates of grid points, and $r_{i,j}^{(1)}, r_{i,j}^{(2)}, r_{i,j}^{(3)}, r_{i,j}^{(4)}$ are independent random variables sampled from a normal distribution. The IC is normalized in the same way as mentioned in the RD case. We attempt to learn the dynamics given different ICs and viscosities. Similar to the RD cases, the parameter space \mathbb{R}^d is also high-dimensional ($d = 6,562$), as the IC is parameterized by 9^4 independent random variables and the scalar viscosity can also vary in range $[0.02, 0.07]$. The reference solution is generated by solving the Burgers' equations on the domain of $(x, y) \in [0, 3.2]^2$, discretized by a fine mesh of 256×256 grids using finite difference method, using a 3^{rd} order accuracy up-wind scheme for the convection term and 6^{th} order accuracy central difference scheme for the diffusion term. Forward Euler method is used for the time stepping, with a timestep of $\delta t = 1 \times 10^{-4}$. Similar to RD case, the reference solution snapshots are collected for DNN training at every other 200 numerical timesteps ($\Delta t = 200 \delta t$). The training dataset consists of sparse reference solutions of six different ν , and there are 36 randomly generated ICs for each ν . In total, the training dataset includes 216 trajectories and each trajectory includes 100 snapshots covering the temporal range of $T = 100 \Delta t$, started from the first numerical step. In PPNN, the PDE-preserving portion is defined on a coarse mesh of size 32×32 with the same learning stepsize as the trainable part ($\Delta t' = \Delta t = 200 \delta t$).

The velocity magnitude contours of the 2D Burgers' equation with different testing parameters are shown in figure 5, obtained by the reference numerical solver (Fig. 5 (a)), PPNN (Fig.

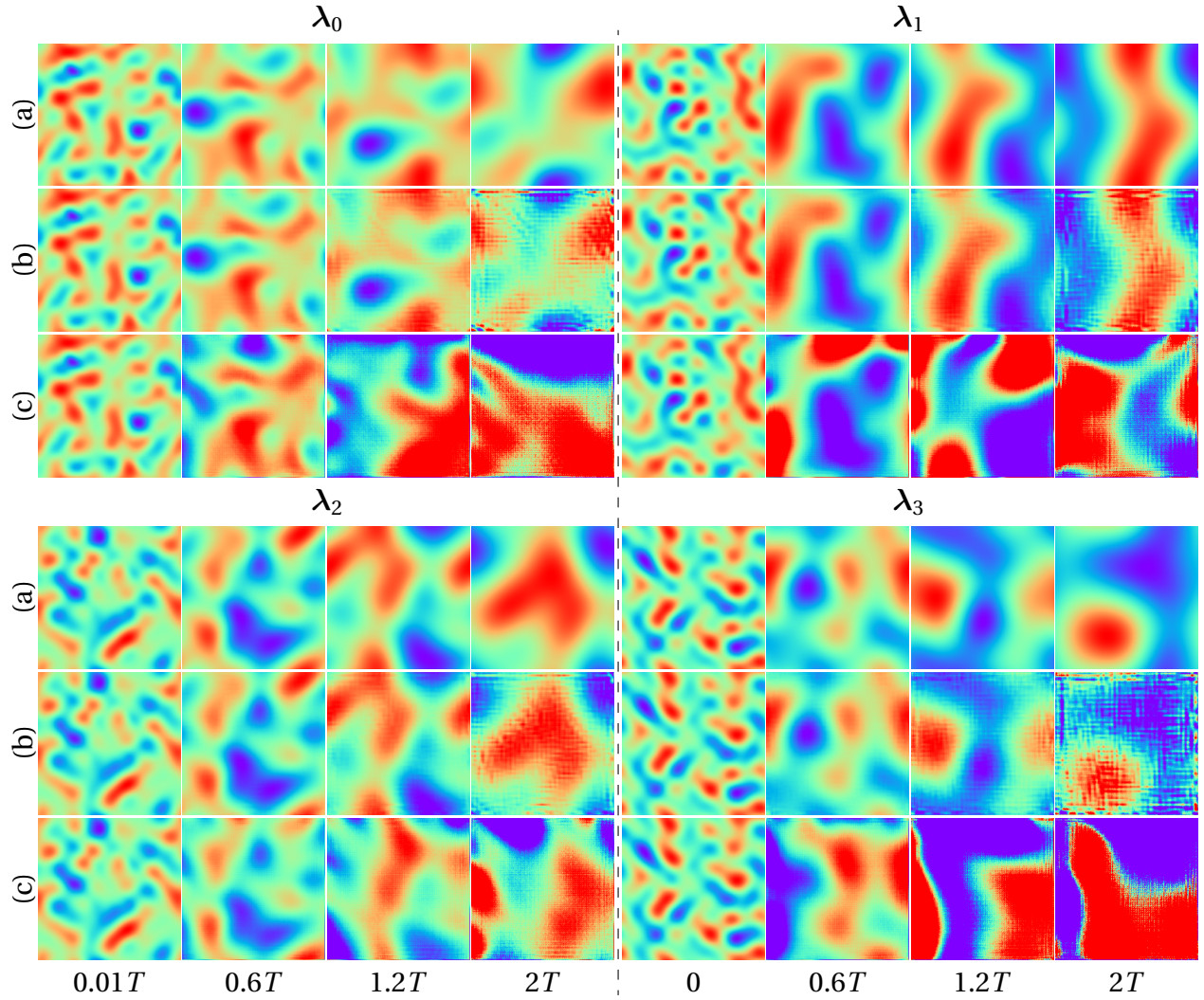


Figure 5: Predicted solution snapshots of velocity magnitude $\|\mathbf{u}\|_2$ for the Burgers equation at different time steps obtained by (b) PPNN (Our method); (c) black-box ConvResNet (baseline model), compared against ground truth (high-resolution FD simulation). $\lambda_0, \lambda_1, \lambda_2$ and λ_3 represent 4 randomly selected testing (unseen) parameters.

5(b)), and black-box baseline (Fig. 5(c)), respectively. Note that all the testing parameters are not seen during training. Similar to the RD case, PPNN shows a significant improvement over the blackbox baseline in terms of long-term rollout error accumulation and generalizability on unseen ICs and viscosity ν . Due to the strong convection effect, blackbox baseline predictions deviate from the reference very quickly, and significant discrepancies in spatial patterns can be observed as early as $t < 0.6T$. In general, the black-box baseline notably suffers from the poor out-of-sample generalizability for unseen parameters, making the predictions useless. Our PPNN significantly outperforms the blackbox baseline, and its prediction results agree with the reference for all testing samples. Although slight prediction noises are present after a long-term model rollout ($t > 1.2T$), the overall spatial patterns can be accurately captured by the PPNN even at the last learning step ($t = 2T$).

The error propagation of both models is given in Fig.6, where the rollout errors ϵ_t at each time step, averaged over 100 randomly selected parameters from training and testing sets, are plotted. Fig.6(a) shows the averaged model rollout error evaluated on 100 training parameters

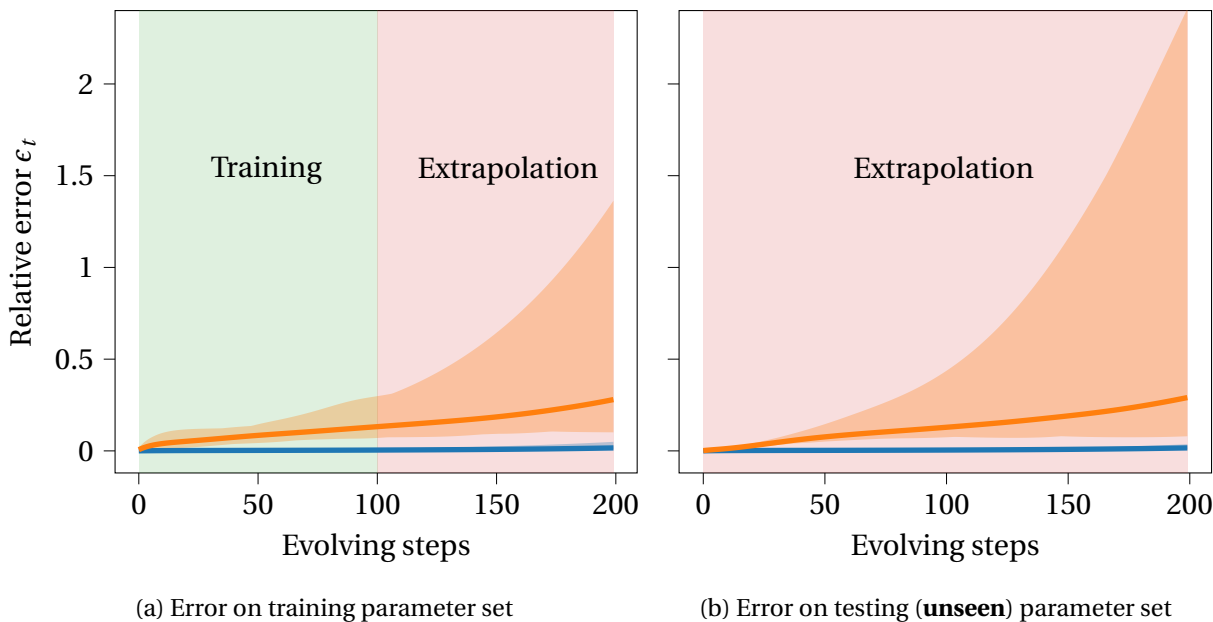


Figure 6: Relative prediction error ϵ_t of PPNN (—) and black-box ConvResNet baseline (—) for the Burgers' equation, averaged on 100 randomly sampled (a) training parameters and (b) testing (*unseen*) parameters. The shaded area shows the scattering of the errors for all trajectories (PPNN range is too small to be visible).

while Fig.6(b) shows the error averaged on 100 randomly generated parameters, which are not used for training. As both models are only trained with the $1T$ ($100\Delta t$) time steps for each parameter in the training set, it is clear that the error of the black-box model grows rapidly once stepping into the extrapolation range $[T, 2T]$ (Fig.6(a)). The error accumulation effect of the black-box model becomes more obvious for those parameters which are not in the training set ((Fig.6(b)) due to the poor generalizability. In contrast, the error of PPNN predictions remains surprisingly low even in the extrapolation range for both training and testing, and there is nearly no error accumulation at all. In addition, the error scattering notably shrinks compared to that of the black-box model, indicating significantly better accuracy, generalizability and robustness of the PPNN compared to the blackbox baseline.

3.3. 2D Navier-Stocks equation

The last case investigates the performance of PPNN to learn an unsteady fluid system exhibiting complex vortex dynamics, which is governed by the 2D parametric unsteady Navier-Stocks (N-S) equations:

$$\begin{aligned} \frac{\partial \mathbf{u}}{\partial t} + \mathbf{u} \cdot \nabla \mathbf{u} &= -\nabla p + \nu \nabla^2 \mathbf{u}, \quad t \in [0, T], \\ \nabla \cdot \mathbf{u} &= 0, \end{aligned} \tag{14}$$

where $\mathbf{u} = [u(x, y, t), v(x, y, t)]^T \in \mathbb{R}^2$ is the velocity vector, $p(x, y, t) \in \mathbb{R}$ is the pressure, and $\nu = 1/Re$ represents the kinematic viscosity (Re is the Reynolds number). The N-S equations are solved in a 2D rectangular domain $(x, y) \in [0, 4] \times [0, 1]$, where a jet with dynamically-changed jet angle is placed at the inlet. Namely, the inflow boundary is defined by a prescribed velocity profile $\mathbf{u}(0, y, t)$,

$$\mathbf{u}(0, y, t) = \begin{bmatrix} u(0, y, t) \\ v(0, y, t) \end{bmatrix} = \begin{bmatrix} \exp(-50(y - y_0)^2) \\ \sin(t) \cdot \exp(-50(y - y_0)^2) \end{bmatrix} \tag{15}$$

where y_0 represents the vertical position of the center of the inlet jet. The outflow boundary condition is set as pressure outlet with a reference pressure of $p(4, y, t) = 0$. No-slip boundary conditions are applied on the upper and lower walls. In this case, the neural network models are expected to learn the fluid dynamics with varying Reynolds number Re and jet locations

y_0 . Namely, a two-dimensional physical parameter vector $\lambda = [Re, y_0]^T$ is considered. In training set, we use five different Re evenly distributed in the range $[2 \times 10^3, 1 \times 10^4]$ and 9 different jet locations y_0 uniformly selected from 0.3 to 0.7. To obtain the reference solution, the N-S equation is solved on a fine mesh of 400×100 grids using the Pressure-Implicit with Splitting of Operators (PISO) algorithm [72] with the numerical timestep of $\delta t = 0.01$. The reference snapshots are collected every other 20 numerical steps, beginning from the 160^{th} step, to form the training trajectory. Namely, the learning step is set as $\Delta t = 20\delta t$. In the training set, there are 45 trajectories, each of which includes 73 snapshots covering the total time of $T = 73\Delta t$. The same FVM discretization scheme is used to construct the PDE-preserving portion, which is defined on a coarse mesh of size 100×25 and operated by several sub-iterations with a stepsize of $\Delta t' = 2\delta t$. All the numerical discretizations are conducted using OpenFOAM, which is an open-source C++ library for FVM.

Figure 7 shows the snapshots of velocity magnitude of the NS equations at two representative testing parameters, which are not seen in the training set. To be specific, $\lambda_0 = [2500, 0.325]^T$ represents a relatively low Reynolds number $Re = 2500$ with the jet located at $y_0 = 0.325$, while $\lambda_1 = [8500, 0.575]^T$ is a higher Reynolds number case ($Re = 8500$) with the jet located at $y_0 = 0.325$. The rollout prediction results of the PPNN (Fig. 7(b)) and baseline black-box ConvResNet (Fig. 7(c)) are compared with the ground truth reference (Fig. 7(a)). Although both models can accurately very capture the spatiotemporal dynamics at the beginning stage (when $t \leq 0.4T$) started from a zero initial flow field, showing excellent predictive performance for the unseen parameters for a short-term rollout, the predictions by the black-box model are soon overwhelmed by the noises due to the rapid error accumulation ($t > T$). However, the proposed PPNN significantly outperforms the blackbox baseline as it managed to provide impressively accurate rollout predictions even at the last testing steps ($t = 3T$), which extrapolate as three times long as the training range, indicating preserving the PDE structure can effectively suppress the error accumulation, which is unavoidable in next-step neural predictors.

To further investigate the error propagation in time for both models, we plot the relative testing errors ϵ_t against time in Fig. 8, which are averaged over 5 randomly selected paramete-

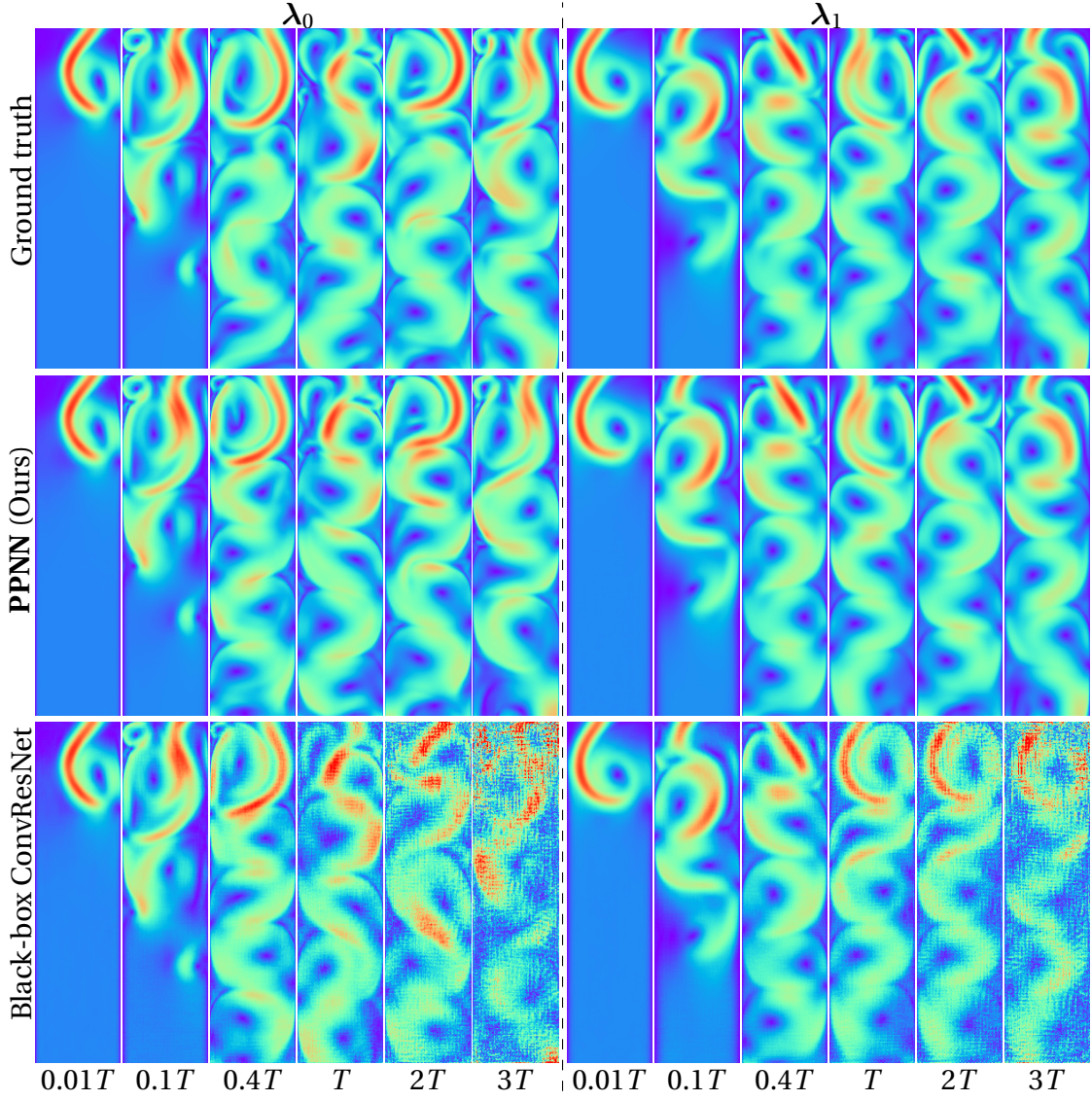


Figure 7: Predicted solution snapshots of velocity magnitude $\|u\|_2$ for the NS equations obtained by PPNN (Ours); black-box ConvResNet (baseline), compared against the ground truth (high-resolution FV simulation), where λ_0 is ($Re = 2500, y_0 = 0.325$), and λ_1 is high Reynolds number ($Re = 8500, y_0 = 0.575$).

ters in both training (Fig. 8(a)) and testing sets (Fig.8(b)). We can clearly see that PPNN managed to maintain an extremely low rollout error in both training and extrapolation ranges, in contrast to the remarkable error accumulation in the black-box baseline results. In particular, the black-box model relative error notably grows only after a short-term model rollout and increases rapidly once it enters the extrapolation range even for testing on the training parameter set (Fig.8(a)), and the errors are accumulated even faster for the testing on unseen parameters (Fig.8(b)). On the contrary, our PPNN has almost no error accumulation and performs much more consistently between the training and extrapolation ranges, with significantly lower rollout errors. The results again demonstrate outstanding predictive accuracy and generalizability of the proposed method. Besides, PPNN also shows a remarkably smaller uncertainty range, indicating great robustness among different testing parameters.

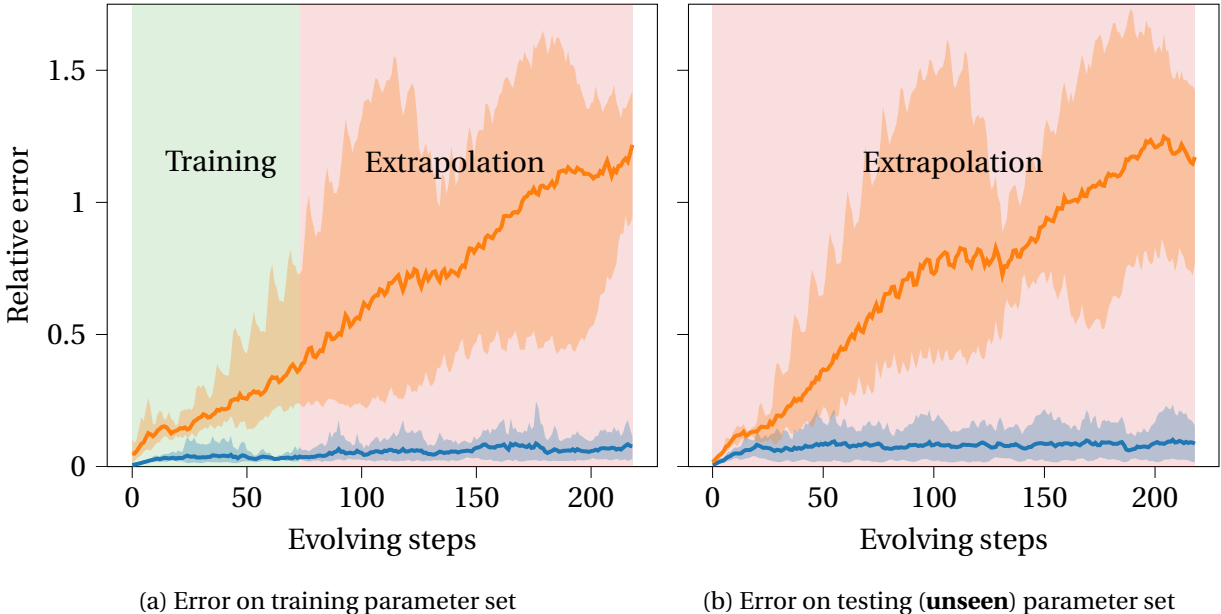


Figure 8: Relative prediction error ϵ_t of PPNN (—) and black-box ConvResNet baseline (—) at different timesteps for the NS equation, averaged on 5 randomly sampled (a) training parameters and (b) testing (*unseen*) parameters. The shaded area shows the scattering of the relative errors over all testing trajectories.

4. Discussion

4.1. When the governing PDEs are partially known

In real-world applications, the underlying physics behind complex spatiotemporal phenomena might not be fully understood, and thus the governing equations can be incomplete, e.g., with unknown source terms, inaccurate physical parameters, or uncertain I/BCs. Such partially-known physics poses great challenges to the traditional simulation paradigm since the governing equations are partially known. Nonetheless, the incomplete prior knowledge can be well utilized in our proposed PPNN framework, where preserving partially-known governing PDE structures can still bring significant merits to data-driven spatiotemporal learning and prediction, which will be discussed in this subsection.

4.1.1. RD equations with unknown reaction term

We first revisit the RD equations studied in section 3.1. Here, we consider the scenario where only the diffusion phenomenon is known in the FitzHugh–Nagumo RD dynamics. Namely, the reaction source terms remain unknown and PPNN only preserves the incomplete RD equations, i.e., 2D diffusion equations,

$$\frac{\partial \mathbf{u}}{\partial t} = \gamma \nabla^2 \mathbf{u}. \quad (16)$$

All the case settings remain the same as those in section 3.1.

Although incomplete/inaccurate prior knowledge about the RD system is preserved, our PPNN still shows a significant advantage over the black-box baseline. Figure 9 compares the snapshots of reactant u at two randomly selected unseen parameters λ_4 and λ_5 predicted by PPNN with the complete RD equation preserved (Fig.9(b)), PPNN with the diffusion terms preserved only (Fig.9(c)), and black-box baseline model (Fig.9(d)). The PPNNs preserving either complete or incomplete RD equations accurately capture the overall patterns and well agree with the reference solutions (Fig.9(a)), while the black-box baseline shows notable discrepancy and large errors, particularly at $t = 2T$, which is the twice of the training phase length. At the last extrapolation step, the prediction results in Fig.9(c) show some visible noise and are less smooth compared to the results by preserving the complete RD equation in Fig.9(b), indicating

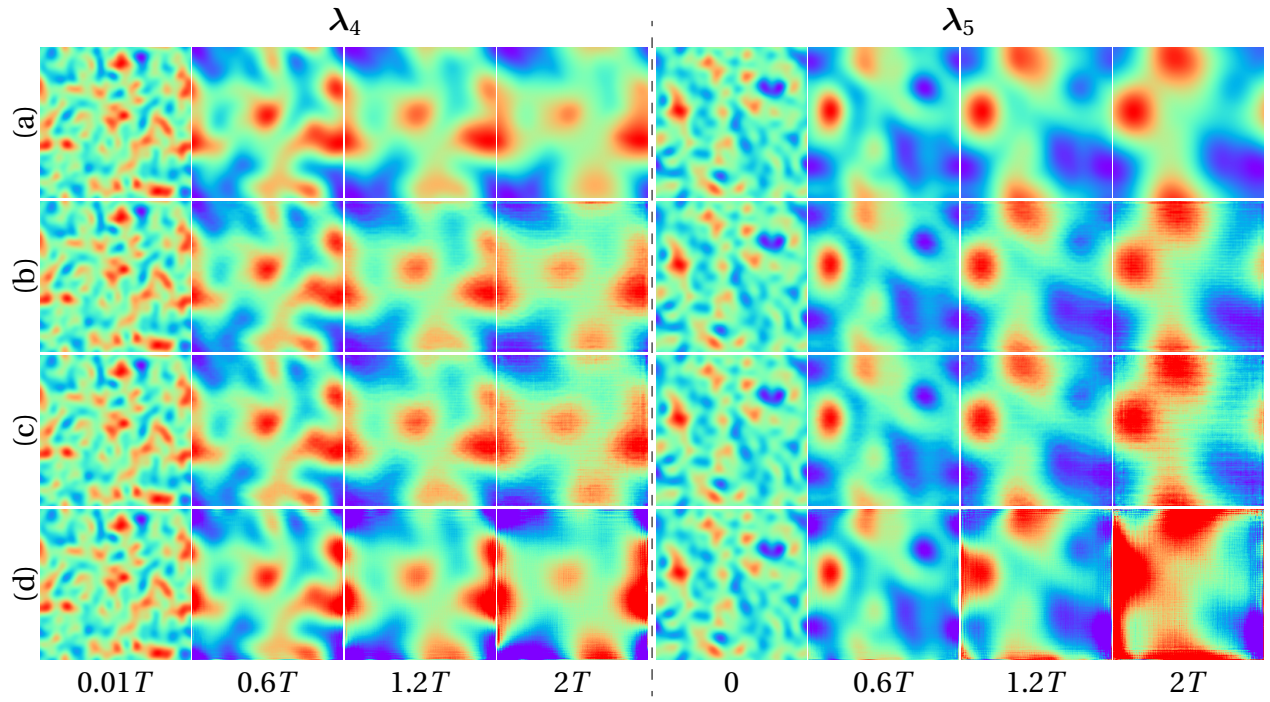


Figure 9: Predicted solution snapshots of u for the RD equations at different time steps and unseen parameters, obtained by (b) PPNN (preserving complete FitzHugh–Nagumo RD equations), (c) PPNN (preserving diffusion terms only), and (d) black-box ConvResNet (baseline model), compared against ground truth. λ_4 and λ_5 are two randomly selected testing (unseen) parameters.

that lack of the prior information on the reactive terms could slightly reduce the improvement by PPNN.

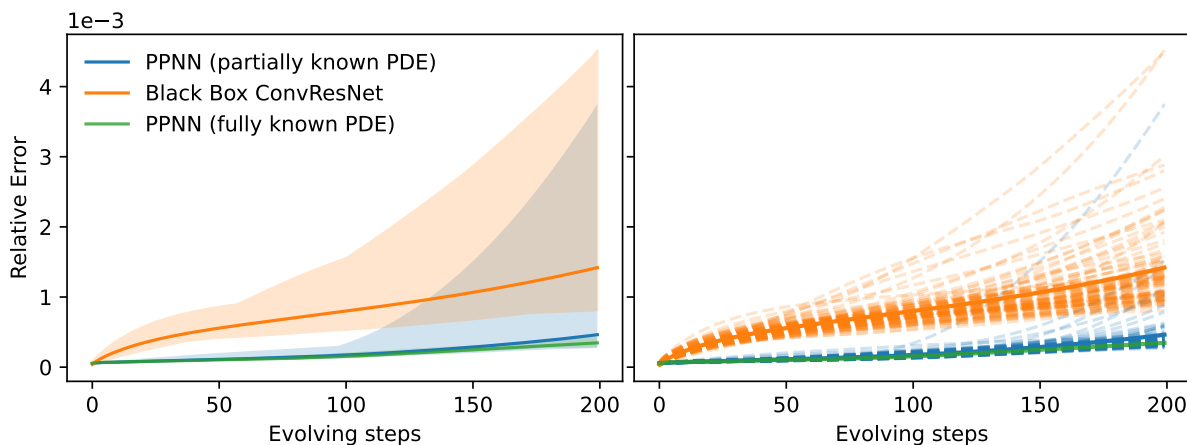


Figure 10: Averaged relative testing error ϵ_t of the PPNN with incomplete PDE, PPNN with complete PDE, and Black-Box ConvResNet baseline for the RD dynamics evaluated on 100 randomly generated testing (unseen) parameters. (Left) shaded area indicates envelopes of the maximum and minimum relative errors of all testing trajectories. (right) the dash line indicates the relative error of each test trajectory.

Figure 10 shows the relative model rollout errors averaged over 100 test trajectories, which are not seen in the training set. The shaded area in the left panel shows the error distribution range of these 100 test trajectories. Even the preserved PDEs are not complete/accurate, the mean relative error (blue line) remains almost the same as the PPNN with fully-known PDEs (green line), which is significantly lower than that of the black-box baseline (red line), showing a great advantage of preserving governing equation structures even if the prior physics knowledge is imperfect. Compared to the PPNN with fully-known PDEs, the error distribution range by preserving partially-known PDEs is increased and error ensemble is more scattered, implying slightly decreased robustness. Although the envelope of the error scattering for incomplete PDEs is much larger than that of the case with fully-known PDEs, this is due to a single outlier trajectory, which can be seen in the right panel. In general, the standard deviation of the error ensemble from the PPNN with partially-known PDE ($\sigma = 1.123 \times 10^{-4}$) is still significantly lower than that of the black-box baseline ($\sigma = 3.412 \times 10^{-4}$). In comparison, the standard deviation of errors in PPNN with fully-known PDEs over the 100 test trajectories is 0.854×10^{-4} .

4.1.2. 2D Naiver-Stocks equation with an unknown magnetic field

In the second case, we consider the the complex magnetic fluid dynamic system governed by Naiver-Stocks equation with an unknown magnetic field:

$$\begin{aligned} \frac{\partial \mathbf{u}}{\partial t} + \mathbf{u} \cdot \nabla \mathbf{u} &= -\nabla p + \nu \nabla^2 \mathbf{u} + \mathbf{F}, \\ \nabla \cdot \mathbf{u} &= 0, \end{aligned} \quad (17)$$

where $\mathbf{u} = [u, v]^T$ is the velocity vector; p is the pressure; while ν represents the kinematic viscosity. Here $\mathbf{F} = [F_x, F_y]^T$ represents the body force introduced by a magnetic field:

$$\begin{aligned} F_x &= mH \frac{\partial H}{\partial x}, & F_y &= mH \frac{\partial H}{\partial y} \\ H(x, y) &= \exp \left[-8 \left((x - L/2)^2 + (y - W/2)^2 \right) \right] \end{aligned} \quad (18)$$

where $m = 0.16$ is the magnetic susceptibility, and H is a time-invariant magnetic intensity. Fig-

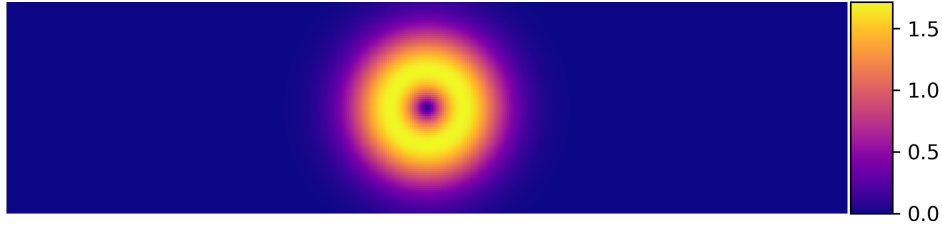


Figure 11: The magnitude of the magnetic field applied to the 2D flow.

ure 11 shows the magnitude of the body force source term. In this case, the magnetic field remains unknown and PPNN only preserves the N-S equation without the magnetic source term. All the other case settings remain unchanged as in section 3.3

Similar to what we observed in Section 4.1.1, the PPNN still remains a significant advantage over the black-box baseline even by preserving an incomplete physics. Figure 12 shows the velocity magnitude $\|\mathbf{u}\|$ results of the flow with or without a magnetic field at the same testing parameter ($\lambda = [Re = 9000, y_0 = 0.475]^T$), predicted by the PPNN and black-box ConvResNet, compared against the reference solution. For both scenarios, only the NS equation portion is preserved in the PPNN, i.e., the magnetic field remains unknown. Figure 12(left) shows the solution snapshots for the flow without the magnetic field (i.e., PPNN preserving the complete

physics), while Figure 12(right) shows the predictions of the flow within the magnetic field (i.e., PPNN preserving an incomplete physics). Comparing the reference solutions at left and right panels, the spatiotemporal patterns of the flow fields exhibit notable differences for the cases with and without magnetic fields. In both scenarios, the blackbox baseline model suffers from the long-term model rollout, particularly for the flow within the magnetic field, the blackbox baseline completely fails to capture the physics when $t > 2T$. In both scenarios, the PPNN remarkably outperforms the black-box baseline. In particular at the last time step $t = 3T$, which is three times the training phase length, the black-box predictions are totally overwhelmed by noise, while our PPNN predictions still agree with the reference very well. Compared to the case preserving the complete physics (Fig. 12 left), a slight deviation from the reference solution can be observed in the PPNN predictions of the flow with an unknown magnetic field (Fig. 12 right), indicating that incomplete prior knowledge could slightly affect the PPNN performance negatively. Nonetheless, preserving the partially-known PDE structure still brings significant merit.

The error propagation is shown in Fig. 13. The relative model rollout errors are averaged over 5 randomly selected unseen parameters for the systems with (Fig. 13 left) and without (Fig. 13 right) the magnetic field. Comparing to the PPNN with completely-known PDEs, the PPNN preserving incomplete/inaccurate prior knowledge does show a slight increment in the mean relative error ϵ_t as well as the error scattering, which implies a slight decrease in the robustness. However, the significant advantage over the black-box baseline remains, and almost no error accumulation is observed in PPNN for both scenarios.

4.2. Training & inference cost

We have demonstrated that the proposed PPNN significantly improves the accuracy, generalizability, and robustness of next-step neural predictors by preserving the mathematical structure of the governing PDEs. Since the PPNN has a more complex network structure than the black-box baseline, it is worthwhile to discuss the training and inference costs of the PPNN and its comparison with the corresponding black-box baseline and the reference numerical solvers.

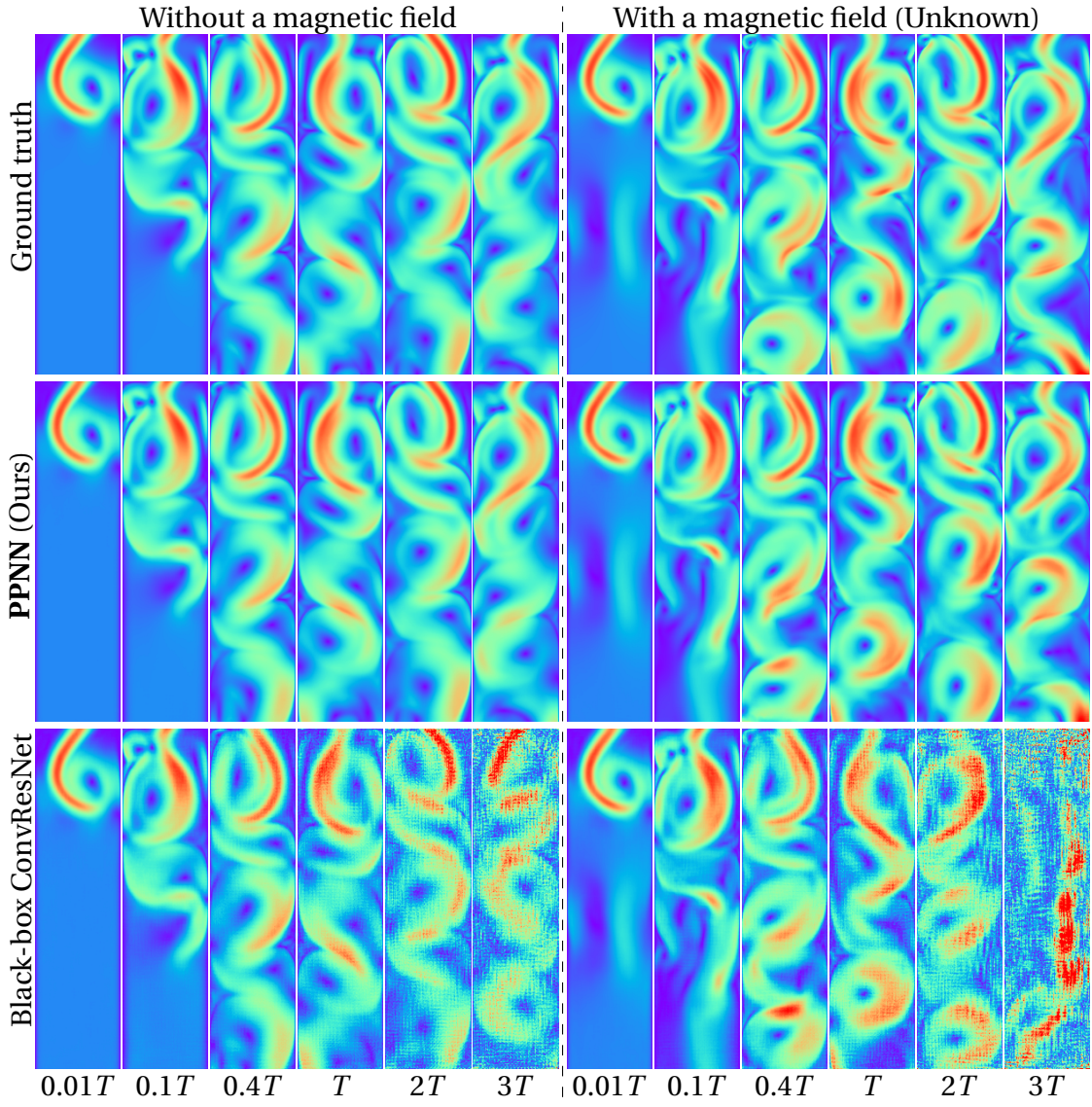


Figure 12: Predicted solution snapshots of flow velocity magnitude $\|u\|_2$ obtained by PPNN (ours); black-box ConvResNet (baseline), compared against ground truth (high-resolution FV simulation) of the NS equations (left) without and (right) with an unknown magnetic source term. The PPNN only preserves a NS equation portion for both scenarios, which are at the same testing (unseen) parameter $\lambda = [9000, 0.475]^T$, which is not in the training set.

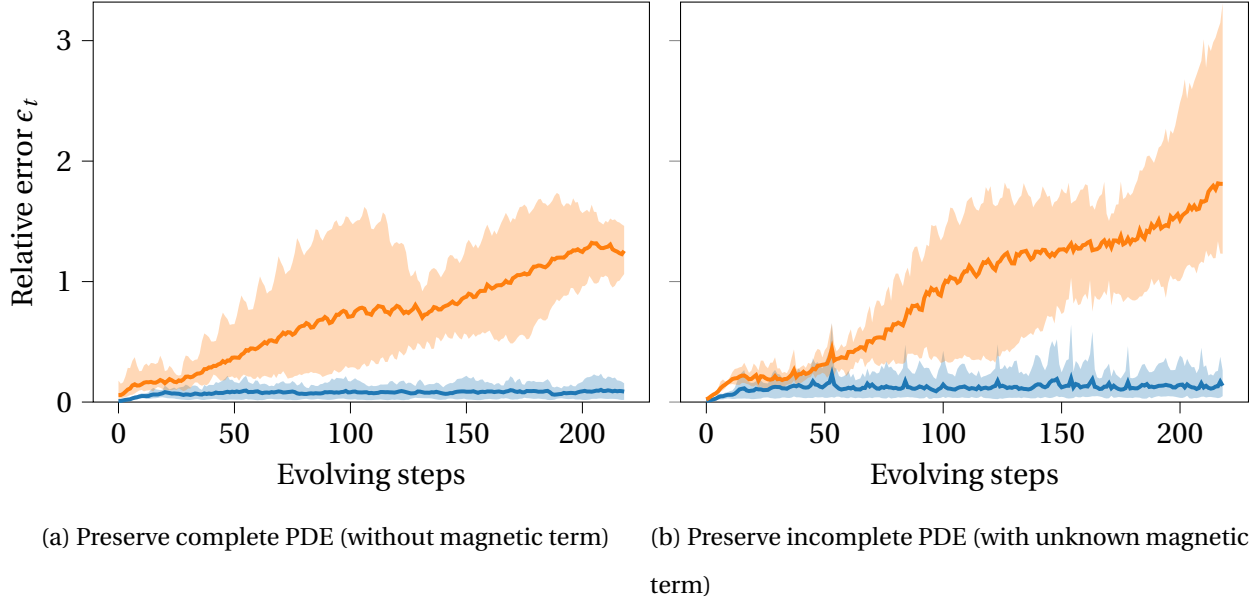


Figure 13: Relative prediction errors ϵ_t of the PPNN (—) and black-box ConvResNet baseline (—) for the NS equation with (b) and without (a) a unknown magnetic body force, averaged on five randomly sampled unseen parameters. The shaded area shows the scattering of relative errors for all testing trajectories.

Training cost. As shown in Fig. 14, the averaged relative (rollout) prediction error ϵ_T on n testing parameters λ at the last time step T in the training process ($n = 8$ in RD, $n = 6$ in Burgers, $n = 5$ in NS). For all the cases, PPNN features a significantly (orders of magnitude) lower error than the blackbox model from a very early training stage. This means that, to achieve the same (if not higher) level of accuracy, our PPNN requires remarkably less training cost compared to the black-box baseline. In addition, under the same training budget, the PPNN is much more accurate than the black-box baseline, demonstrating the merit of PPNN by leveraging the prior knowledge for network architecture design.

Inference cost. The inference costs of different neural networks and numerical solvers on the three testing cases (Sec 3) with the model rollout length of T are summarized in Table 1. Due to the fast inference speed of neural networks, both next-step neural models show significant speedup compared to the high-fidelity numerical solvers. In particular, the speedup by the PPNN varies from $10\times$ to $60\times$ without notably sacrificing the prediction accuracy. Such speedup

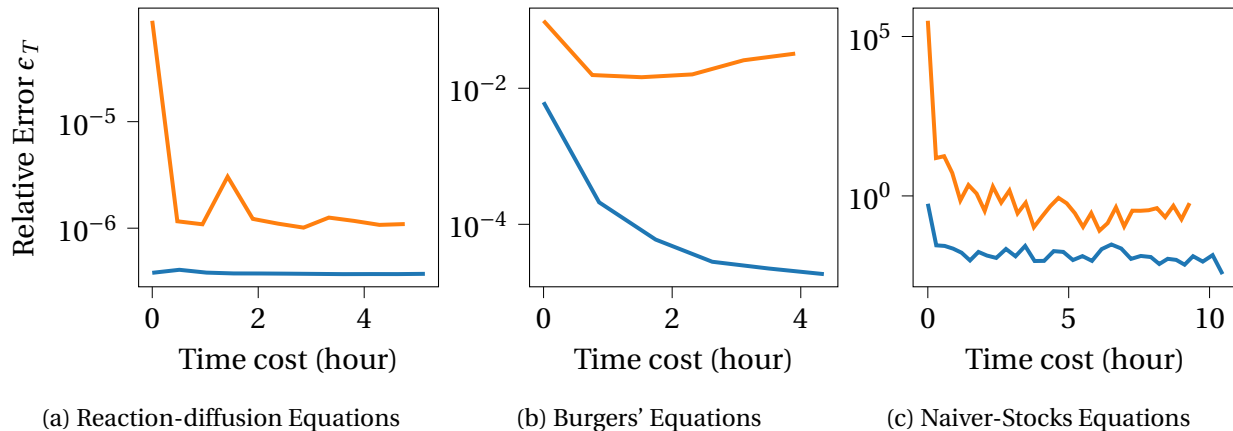


Figure 14: Averaged relative test error at the last time step ϵ_T of PPNN (—) and black-box ConvResNet (—) in training process of different cases in section 3

will become more tremendous considering a longer model rollout and enormous repeated model queries on a large number of different parameter settings, which are commonly required in many-query applications such as optimization design, inverse problems, and uncertainty quantification. Note that all models are compared on the same hardware (GPU or CPU) to eliminate the difference introduced by hardware. However, as most legacy numerical solvers can only run on CPUs, the speedup by neural models can be much more remarkable if they leverage massive GPU parallelism. Admittedly, adding the PDE-preserving part inevitably increases the inference cost compared to the blackbox baseline, but the huge performance improvement by doing so outweighs the slight computational overhead, as demonstrated in sec 3. We have to point out that the computation of the PDE-preserving portion is not fully optimized, particularly in the NS case, where low-speed I/O interactions reduce the overall speedup ratio compared to the numerical solver based on the mature CFD platform OpenFOAM. Further performance improvements are expected by customized code optimizations in future work.

4.3. The relationship between the PDE-preserving portion and numerical solvers

The advantages of the proposed PPNN over the pure blackbox baseline mainly come from baking the prior knowledge into the network architecture. As discussed above, the mathematical structures of the governing physics are encoded into the PPNN based on the relationship

Table 1: Inference cost (model query cost)

Governing equation	Time cost (seconds)		
	Numerical Solver	PPNN	Black-box ConvResNet
RD *	28.6467	3.1854	3.0489
Burgers *	70.8707	3.3093	3.1491
NS **	6621.6352	116.6499	25.3653

* Test on NVIDIA GeForce RTX 3070; number in the table shows the time cost of testing 10 trajectories.

** Test on a single core of Intel Xeon Gold 6138; number in the table shows the time cost of testing 1 trajectory.

between neural network structures and differential equations. From the numerical modeling perspective, if our understanding of the underlying physics is complete and accurate (i.e., complete governing PDEs are available), the PDE-preserving portion in PPNN can be interpreted as a numerical solver with the explicit forward Euler scheme defined on a coarse mesh. For simplicity, we here refer to this numerical solver derived from the fully-known PDE preserving part as the “coarse solver”. It is interesting to see how well it performs by the coarse solver only when governing equations and IC/BCs are fully known. We use the NS case as an example. Figure 15 shows the magnitude of velocity $\|\mathbf{u}\|$ predicted by the PPNN, black-box ConvResNet and coarse solver, respectively, compared against the reference solution. Two representative testing parameters are studied here, one is at a lower Reynolds number $Re = 2500$, $y_0 = 0.325$ (Fig. 15 left), and the other is at a higher Reynolds number $Re = 9000$, $y_0 = 0.475$ (Fig. 15 right). It’s clear that the predictions by the coarse solver notably deviate from the reference solution from $0.4T$, and most vortices are damped out due to the coarse spatial discretization. This becomes worse in the Reynolds number scenario, where the coarse solver predicted flow field is unphysical at $0.1T$ and the simulation completely diverged at $t = 1.16T$, because of the large learning timestep making traditional numerical solvers fail to satisfy the stability constraint.

As shown in the error propagation curves in Fig. 16, the coarse solver has large prediction errors over the testing parameter set from the very beginning, which is much higher than that of

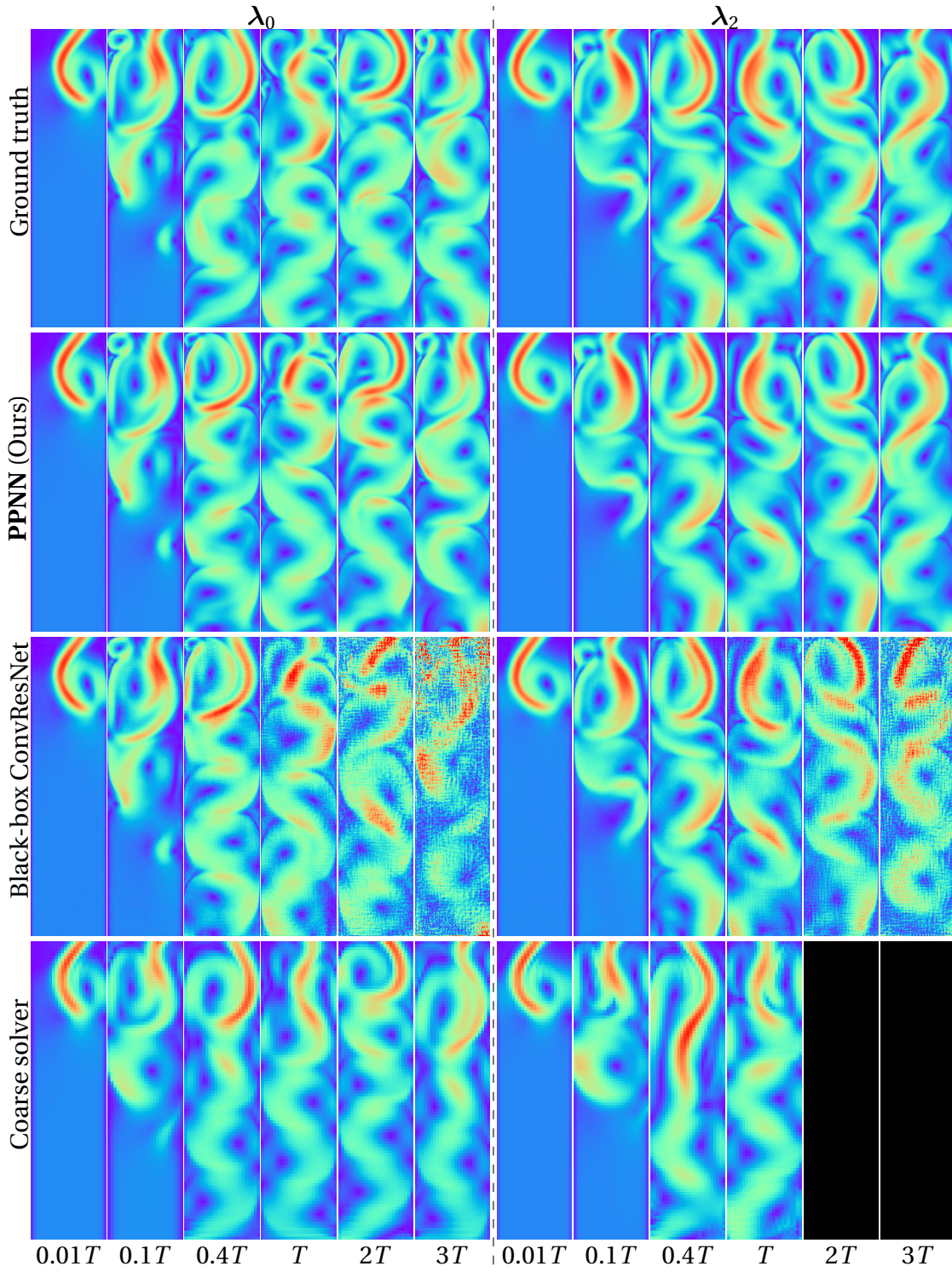


Figure 15: Predicted solution snapshots of velocity magnitude $\|u\|_2$ for the NS equations, obtained by PPNN (ours); black-box ConvResNet (baseline), and only PDE-preserving part (coarse solver), compared against ground truth (high-resolution FV simulation), where $\lambda_0 = [2500, 0.325]^T$ and $\lambda_2 = [9000, 0.475]^T$, which are unseen in the training set. The black color indicates NaN, i.e., solution blow up.

the blackbox data-driven baseline. Since several of the testing trajectories by the coarse solver diverges quickly after 70 evolving steps, the error propagation curve stops. This figure again

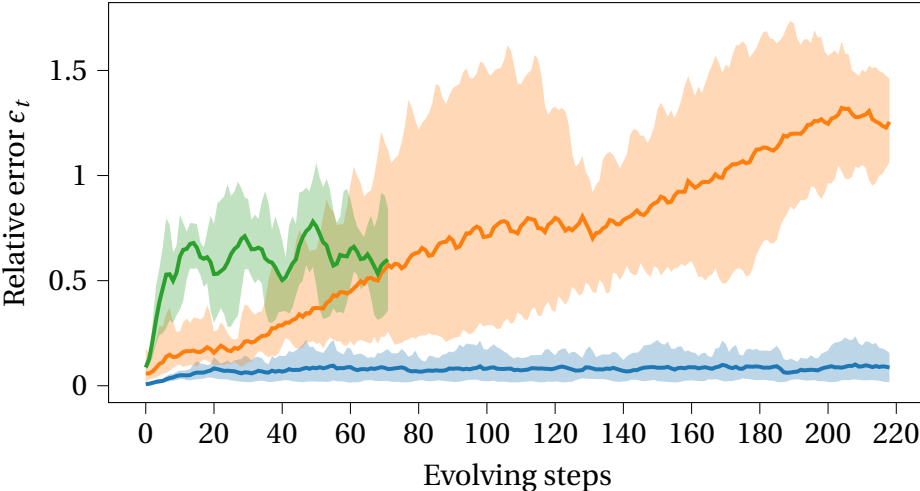


Figure 16: Relative error at different time steps of PPNN (—), Black-Box neural network (—) and the coarse solver (—) compared to the ground truth results obtained by icoFoam on a fine mesh. The relative error is an averaged value of 5 test trajectories with randomly sampled parameters, these parameters not in the training set. The shaded area shows the maximum and minimum relative error of these testing trajectories. In coarse solver, 2 of the testing trajectories diverged (*NaN*) at the 72nd step thus the curve (—) stops at 71st step

empirically demonstrates that the PPNN structure not only overcomes the error accumulation problem in black-box methods, but also significantly outperforms numerical solvers by simply coarsen the spatiotemporal grids. On the other hand, for those trajectories that do not diverge, the coarse solver’s relative errors are limited to a certain level, which is in contrast to black-box, data-driven methods where the error constantly grows due to the error accumulation. This phenomenon implies that preserving PDEs plays a critical role in addressing the issue of error accumulation, which does not simply provide a rough estimation of the next step, but carries underlying physics information that guides the longer-term prediction.

5. Conclusion

In this work, we proposed a novel physics-inspired deep learning architecture, PDE-preserved neural network (PPNN), aiming to learn parametric spatiotemporal physics, where the (par-

tially) known governing PDE structures are preserved via convolutional residual connection blocks in a multi-resolution setting. The PDE-preserving ConvResNet blocks together with trainable ConvResNet blocks in an encoding-decoding manner bring the PPNN significant advantages in long-term model rollout accuracy, generalizability in spatiotemporal and parameter space, and training efficiency. The effectiveness and merit have been demonstrated over a handful of challenging spatiotemporal prediction tasks, including the FitzHugh–Nagumo reaction diffusion equations, viscous Burgers equations and Naiver-Stocks equations, compared to the existing state-of-the-art black-box next-step neural operator. Moreover, PPNN demonstrated its capability in leveraging physics prior knowledge to significantly improve the learning/prediction performance even if the preserved physics is incomplete or inaccurate. Finally, the inference and training costs of the proposed model are discussed, and the role of the PDE-preserving portion of PPNN is investigated. The proposed methods have promising potential to serve as a reliable surrogate model for spatiotemporal dynamics in many applications that require repeated model queries, e.g., design optimization, inverse problems, data assimilation, and uncertainty quantification. In addition, this work explored a new direction of leveraging physics-induced bias in SciML and showcased how to use physical prior knowledge to inform learning architecture design, which shed new light on physics-informed deep learning from a different aspect.

Acknowledgment

The authors would like to acknowledge the funds from National Science Foundation, United States of America under award numbers CMMI-1934300 and OAC-2047127, the Air Force Office of Scientific Research (AFOSR), United States of America under award number FA9550-22-1-0065, and startup funds from the College of Engineering at University of Notre Dame in supporting this study.

References

- [1] H. F. Lui, W. R. Wolf, Construction of reduced-order models for fluid flows using deep feed-forward neural networks, *Journal of Fluid Mechanics* 872 (2019) 963–994.

- [2] O. San, R. Maulik, M. Ahmed, An artificial neural network framework for reduced order modeling of transient flows, *Communications in Nonlinear Science and Numerical Simulation* 77 (2019) 271–287.
- [3] P. Wu, J. Sun, X. Chang, W. Zhang, R. Arcucci, Y. Guo, C. C. Pain, Data-driven reduced order model with temporal convolutional neural network, *Computer Methods in Applied Mechanics and Engineering* 360 (2020) 112766.
- [4] H. Gao, J.-X. Wang, M. J. Zahr, Non-intrusive model reduction of large-scale, nonlinear dynamical systems using deep learning, *Physica D: Nonlinear Phenomena* 412 (2020) 132614.
- [5] S. Fresca, A. Manzoni, Real-time simulation of parameter-dependent fluid flows through deep learning-based reduced order models, *Fluids* 6 (7) (2021) 259.
- [6] S. Fresca, A. Manzoni, Pod-dl-rom: enhancing deep learning-based reduced order models for nonlinear parametrized pdes by proper orthogonal decomposition, *Computer Methods in Applied Mechanics and Engineering* 388 (2022) 114181.
- [7] T. Murata, K. Fukami, K. Fukagata, Nonlinear mode decomposition with convolutional neural networks for fluid dynamics, *Journal of Fluid Mechanics* 882 (2020).
- [8] J.-Z. Peng, S. Chen, N. Aubry, Z. Chen, W.-T. Wu, Unsteady reduced-order model of flow over cylinders based on convolutional and deconvolutional neural network structure, *Physics of Fluids* 32 (12) (2020) 123609.
- [9] A. T. Mohan, D. Tretiak, M. Chertkov, D. Livescu, Spatio-temporal deep learning models of 3d turbulence with physics informed diagnostics, *Journal of Turbulence* 21 (9-10) (2020) 484–524.
- [10] K. Lee, K. T. Carlberg, Model reduction of dynamical systems on nonlinear manifolds using deep convolutional autoencoders, *Journal of Computational Physics* 404 (2020) 108973.

- [11] R. Maulik, B. Lusch, P. Balaprakash, Reduced-order modeling of advection-dominated systems with recurrent neural networks and convolutional autoencoders, *Physics of Fluids* 33 (3) (2021) 037106.
- [12] K. Fukami, K. Hasegawa, T. Nakamura, M. Morimoto, K. Fukagata, Model order reduction with neural networks: Application to laminar and turbulent flows, *SN Computer Science* 2 (6) (2021) 1–16.
- [13] M. Morimoto, K. Fukami, K. Zhang, A. G. Nair, K. Fukagata, Convolutional neural networks for fluid flow analysis: toward effective metamodeling and low dimensionalization, *Theoretical and Computational Fluid Dynamics* 35 (5) (2021) 633–658.
- [14] T. Pfaff, M. Fortunato, A. Sanchez-Gonzalez, P. Battaglia, Learning mesh-based simulation with graph networks, in: *International Conference on Learning Representations*, 2020.
- [15] X. Han, H. Gao, T. Pfaff, J.-X. Wang, L. Liu, [Predicting physics in mesh-reduced space with temporal attention](#), in: *International Conference on Learning Representations*, 2022.
URL <https://openreview.net/forum?id=XctLdNfCmP>
- [16] N. Baker, F. Alexander, T. Bremer, A. Hagberg, Y. Kevrekidis, H. Najm, M. Parashar, A. Patra, J. Sethian, S. Wild, et al., Workshop report on basic research needs for scientific machine learning: Core technologies for artificial intelligence, Tech. rep., USDOE Office of Science (SC), Washington, DC (United States) (2019).
- [17] M. Raissi, P. Perdikaris, G. E. Karniadakis, Physics-informed neural networks: A deep learning framework for solving forward and inverse problems involving nonlinear partial differential equations, *Journal of Computational physics* 378 (2019) 686–707.
- [18] L. Sun, H. Gao, S. Pan, J.-X. Wang, Surrogate modeling for fluid flows based on physics-constrained deep learning without simulation data, *Computer Methods in Applied Mechanics and Engineering* 361 (2020) 112732.

- [19] R. Zhang, Y. Liu, H. Sun, Physics-informed multi-lstm networks for metamodeling of non-linear structures, *Computer Methods in Applied Mechanics and Engineering* 369 (2020) 113226.
- [20] E. Haghighat, M. Raissi, A. Moure, H. Gomez, R. Juanes, A physics-informed deep learning framework for inversion and surrogate modeling in solid mechanics, *Computer Methods in Applied Mechanics and Engineering* 379 (2021) 113741.
- [21] L. Sun, J.-X. Wang, Physics-constrained bayesian neural network for fluid flow reconstruction with sparse and noisy data, *Theoretical and Applied Mechanics Letters* 10 (3) (2020) 161–169.
- [22] A. Arzani, J.-X. Wang, R. M. D’Souza, Uncovering near-wall blood flow from sparse data with physics-informed neural networks, *Physics of Fluids* 33 (7) (2021) 071905. doi:10.1063/5.0055600.
- [23] L. Lu, R. Pestourie, W. Yao, Z. Wang, F. Verdugo, S. G. Johnson, Physics-informed neural networks with hard constraints for inverse design, *SIAM Journal on Scientific Computing* 43 (6) (2021) B1105–B1132.
- [24] E. Zhang, M. Dao, G. E. Karniadakis, S. Suresh, Analyses of internal structures and defects in materials using physics-informed neural networks, *Science advances* 8 (7) (2022) eabk0644.
- [25] J. Han, A. Jentzen, E. Weinan, Solving high-dimensional partial differential equations using deep learning, *Proceedings of the National Academy of Sciences* 115 (34) (2018) 8505–8510.
- [26] D. Zhang, L. Lu, L. Guo, G. E. Karniadakis, Quantifying total uncertainty in physics-informed neural networks for solving forward and inverse stochastic problems, *Journal of Computational Physics* 397 (2019) 108850.
- [27] D. Zhang, L. Guo, G. E. Karniadakis, Learning in modal space: Solving time-dependent stochastic pdes using physics-informed neural networks, *SIAM Journal on Scientific Computing* 42 (2) (2020) A639–A665.

- [28] Y. Yang, P. Perdikaris, Adversarial uncertainty quantification in physics-informed neural networks, *Journal of Computational Physics* 394 (2019) 136–152.
- [29] C. Rao, H. Sun, Y. Liu, Physics-informed deep learning for computational elastodynamics without labeled data, *Journal of Engineering Mechanics* 147 (8) (2021) 04021043.
- [30] E. Kharazmi, Z. Zhang, G. E. Karniadakis, hp-vpinns: Variational physics-informed neural networks with domain decomposition, *Computer Methods in Applied Mechanics and Engineering* 374 (2021) 113547.
- [31] A. D. Jagtap, E. Kharazmi, G. E. Karniadakis, Conservative physics-informed neural networks on discrete domains for conservation laws: Applications to forward and inverse problems, *Computer Methods in Applied Mechanics and Engineering* 365 (2020) 113028.
- [32] L. Lu, P. Jin, G. Pang, Z. Zhang, G. E. Karniadakis, Learning nonlinear operators via deep-onet based on the universal approximation theorem of operators, *Nature Machine Intelligence* 3 (3) (2021) 218–229.
- [33] Z. Li, N. B. Kovachki, K. Azizzadenesheli, K. Bhattacharya, A. Stuart, A. Anandkumar, et al., Fourier neural operator for parametric partial differential equations, in: *International Conference on Learning Representations*, 2020.
- [34] S. Wang, H. Wang, P. Perdikaris, Learning the solution operator of parametric partial differential equations with physics-informed deep-onets, *Science advances* 7 (40) (2021) eabi8605.
- [35] A. D. Jagtap, K. Kawaguchi, G. E. Karniadakis, Adaptive activation functions accelerate convergence in deep and physics-informed neural networks, *Journal of Computational Physics* 404 (2020) 109136.
- [36] S. Wang, X. Yu, P. Perdikaris, When and why pinns fail to train: A neural tangent kernel perspective, *Journal of Computational Physics* 449 (2022) 110768.

- [37] S. Wang, S. Sankaran, P. Perdikaris, Respecting causality is all you need for training physics-informed neural networks, arXiv preprint arXiv:2203.07404 (2022).
- [38] H. Gao, L. Sun, J.-X. Wang, PhyGeoNet: physics-informed geometry-adaptive convolutional neural networks for solving parameterized steady-state PDEs on irregular domain, *Journal of Computational Physics* 428 (2021) 110079.
- [39] P. Ren, C. Rao, Y. Liu, J.-X. Wang, H. Sun, Phycrnet: Physics-informed convolutional-recurrent network for solving spatiotemporal pdes, *Computer Methods in Applied Mechanics and Engineering* 389 (2022) 114399.
- [40] Y. Zhu, N. Zabarar, P.-S. Koutsourelakis, P. Perdikaris, Physics-constrained deep learning for high-dimensional surrogate modeling and uncertainty quantification without labeled data, *Journal of Computational Physics* 394 (2019) 56–81.
- [41] N. Geneva, N. Zabarar, Modeling the dynamics of pde systems with physics-constrained deep auto-regressive networks, *Journal of Computational Physics* 403 (2020) 109056.
- [42] H. Gao, L. Sun, J.-X. Wang, Super-resolution and denoising of fluid flow using physics-informed convolutional neural networks without high-resolution labels, *Physics of Fluids* 33 (7) (2021) 073603.
- [43] N. Wandel, M. Weinmann, R. Klein, Teaching the incompressible navier–stokes equations to fast neural surrogate models in three dimensions, *Physics of Fluids* 33 (4) (2021) 047117.
- [44] R. Ranade, C. Hill, J. Pathak, Discretizationnet: A machine-learning based solver for navier–stokes equations using finite volume discretization, *Computer Methods in Applied Mechanics and Engineering* 378 (2021) 113722.
- [45] H. Yao, Y. Gao, Y. Liu, Fea-net: A physics-guided data-driven model for efficient mechanical response prediction, *Computer Methods in Applied Mechanics and Engineering* 363 (2020) 112892.

- [46] S. K. Mitusch, S. W. Funke, M. Kuchta, Hybrid fem-nn models: Combining artificial neural networks with the finite element method, *Journal of Computational Physics* 446 (2021) 110651.
- [47] H. Gao, M. J. Zahr, J.-X. Wang, Physics-informed graph neural galerkin networks: A unified framework for solving pde-governed forward and inverse problems, *Computer Methods in Applied Mechanics and Engineering* 390 (2022) 114502.
- [48] X.-Y. Liu, J.-X. Wang, Physics-informed dyna-style model-based deep reinforcement learning for dynamic control, *Proceedings of the Royal Society A: Mathematical, Physical and Engineering Sciences* 477 (2255) (2021) 20210618. [doi:10.1098/rspa.2021.0618](https://doi.org/10.1098/rspa.2021.0618).
- [49] E. Haber, L. Ruthotto, Stable architectures for deep neural networks, *Inverse problems* 34 (1) (2017) 014004.
- [50] Y. Lu, A. Zhong, Q. Li, B. Dong, Beyond finite layer neural networks: Bridging deep architectures and numerical differential equations, in: *International Conference on Machine Learning*, PMLR, 2018, pp. 3276–3285.
- [51] F. Rousseau, L. Drumetz, R. Fablet, Residual networks as flows of diffeomorphisms, *Journal of Mathematical Imaging and Vision* 62 (3) (2020) 365–375.
- [52] L. Ruthotto, E. Haber, Deep neural networks motivated by partial differential equations, *Journal of Mathematical Imaging and Vision* 62 (3) (2020) 352–364.
- [53] B. Chamberlain, J. Rowbottom, M. I. Gorinova, M. Bronstein, S. Webb, E. Rossi, Grand: Graph neural diffusion, in: *International Conference on Machine Learning*, PMLR, 2021, pp. 1407–1418.
- [54] M. Eliasof, E. Haber, E. Treister, PDE-GCN: Novel architectures for graph neural networks motivated by partial differential equations, *Advances in Neural Information Processing Systems* 34 (2021).

- [55] R. T. Chen, Y. Rubanova, J. Bettencourt, D. K. Duvenaud, Neural ordinary differential equations, *Advances in neural information processing systems* 31 (2018).
- [56] K. He, X. Zhang, S. Ren, J. Sun, Deep residual learning for image recognition, in: *Proceedings of the IEEE conference on computer vision and pattern recognition*, 2016, pp. 770–778.
- [57] A. Gholami, K. Keutzer, G. Biros, Anode: Unconditionally accurate memory-efficient gradients for neural odes, *arXiv preprint arXiv:1902.10298* (2019).
- [58] M. Innes, A. Edelman, K. Fischer, C. Rackauckas, E. Saba, V. B. Shah, W. Tebbutt, A differentiable programming system to bridge machine learning and scientific computing, *arXiv preprint arXiv:1907.07587* (2019).
- [59] C. Rackauckas, Y. Ma, J. Martensen, C. Warner, K. Zubov, R. Supekar, D. Skinner, A. Ramadhan, A. Edelman, Universal differential equations for scientific machine learning, *arXiv preprint arXiv:2001.04385* (2020).
- [60] Y. Sun, L. Zhang, H. Schaeffer, Neupde: Neural network based ordinary and partial differential equations for modeling time-dependent data, in: *Mathematical and Scientific Machine Learning*, PMLR, 2020, pp. 352–372.
- [61] A. Hochlehnert, A. Terenin, S. Sæmundsson, M. Deisenroth, Learning contact dynamics using physically structured neural networks, in: *International Conference on Artificial Intelligence and Statistics*, PMLR, 2021, pp. 2152–2160.
- [62] E. Heiden, D. Millard, E. Coumans, Y. Sheng, G. S. Sukhatme, Neursim: Augmenting differentiable simulators with neural networks, in: *2021 IEEE International Conference on Robotics and Automation (ICRA)*, IEEE, 2021, pp. 9474–9481.
- [63] M. Hackenberg, M. Grodd, C. Kreutz, M. Fischer, J. Esins, L. Grabenhenrich, C. Karagiannis, H. Binder, Using differentiable programming for flexible statistical modeling, *The American Statistician* (2021) 1–10.

- [64] D. Kochkov, J. A. Smith, A. Alieva, Q. Wang, M. P. Brenner, S. Hoyer, Machine learning–accelerated computational fluid dynamics, *Proceedings of the National Academy of Sciences* 118 (21) (2021).
- [65] F. D. A. Belbute-Peres, T. Economon, Z. Kolter, Combining differentiable pde solvers and graph neural networks for fluid flow prediction, in: *International Conference on Machine Learning*, PMLR, 2020, pp. 2402–2411.
- [66] K. Um, R. Brand, Y. R. Fei, P. Holl, N. Thuerey, Solver-in-the-loop: Learning from differentiable physics to interact with iterative pde-solvers, *Advances in Neural Information Processing Systems* 33 (2020) 6111–6122.
- [67] B. Dong, Q. Jiang, Z. Shen, Image restoration: Wavelet frame shrinkage, nonlinear evolution pdes, and beyond, *Multiscale Modeling & Simulation* 15 (1) (2017) 606–660.
- [68] Z. Long, Y. Lu, X. Ma, B. Dong, Pde-net: Learning pdes from data, in: *International Conference on Machine Learning*, PMLR, 2018, pp. 3208–3216.
- [69] Z. Long, Y. Lu, B. Dong, Pde-net 2.0: Learning pdes from data with a numeric-symbolic hybrid deep network, *Journal of Computational Physics* 399 (2019) 108925.
- [70] A. Sanchez-Gonzalez, J. Godwin, T. Pfaff, R. Ying, J. Leskovec, P. Battaglia, Learning to simulate complex physics with graph networks, in: *International Conference on Machine Learning*, PMLR, 2020, pp. 8459–8468.
- [71] A. Paszke, S. Gross, F. Massa, A. Lerer, J. Bradbury, G. Chanan, T. Killeen, Z. Lin, N. Gimelshein, L. Antiga, A. Desmaison, A. Kopf, E. Yang, Z. DeVito, M. Raison, A. Tejani, S. Chilamkurthy, B. Steiner, L. Fang, J. Bai, S. Chintala, Pytorch: An imperative style, high-performance deep learning library, in: H. Wallach, H. Larochelle, A. Beygelzimer, F. d'Alché-Buc, E. Fox, R. Garnett (Eds.), *Advances in Neural Information Processing Systems* 32, Curran Associates, Inc., 2019, pp. 8024–8035.
- [72] R. H. Pletcher, J. C. Tannehill, D. Anderson, *Computational fluid mechanics and heat transfer*, CRC press, 2012.